

Phase-field simulations of nucleation, growth, and coarsening of β_1 precipitates in Mg–Nd alloys

L. Shi¹, S. DeWitt¹, D. Montiel¹, Q. Shi¹, J. Allison¹, and K. Thornton^{1,2,*}

¹Department of Materials Science and Engineering, University of Michigan, Ann Arbor, MI 48109, United States of America

²Department of Nuclear Engineering and Radiological Sciences, University of Michigan, Ann Arbor, MI 48109, United States of America

*Author to whom any correspondence should be addressed.

Email: kthorn@umich.edu

Abstract

The spatial distribution and morphology of precipitates formed during aging are key factors that determine the precipitation hardening response of various magnesium–rare earth alloys. In recent years, the use of high-performance computing clusters and massively parallel frameworks has enabled quantitative simulations of the evolution of individual and multiple precipitates at relevant length and time scales. However, predictive modeling of precipitate evolution remains challenging, in part because many key thermodynamic and kinetic parameters governing the underlying physics are either unknown or have a high degree of uncertainty. In this work, we developed a workflow in which experimental data were used to parameterize a phase-field model to perform two-dimensional (2D) simulations of concurrent nucleation and evolution of β_1 precipitates in magnesium–neodymium alloy during aging. Matrix composition and precipitate number density at different aging times were obtained from atom probe tomography and transmission electron microscopy measurements, respectively. We applied a stereological method to estimate the three-dimensional (3D) number densities from experimental cross-sectional transmission electron micrographs. The estimated 3D number density data were then converted to effective 2D number densities. The effective 2D number density and composition data were used to determine the

required model parameters by minimizing the discrepancy between simulation and experimental results. The parameterized model allows for quantitative phase-field simulations of nucleation and growth of β_1 precipitates, which can be employed to optimize aging time to achieve a target number density of precipitates. This work highlights an approach to overcome the challenges associated with parameterizing a coupled phase-field and nucleation model.

1. Introduction

Magnesium (Mg) alloys hold significant promise as structural materials in the automotive and aerospace industries due to their high strength and low density [1-3]. The demand for lightweight materials is increasing, as they improve fuel efficiency and reduce emissions by enabling significant weight savings in automobiles [4]. The incorporation of rare earth (RE) elements into Mg alloys enhances their mechanical strength and creep resistance [5]. Furthermore, Mg-RE alloys offer excellent oxidation resistance [6] and, in some cases, enhanced corrosion resistance [7], while maintaining low density [2, 8, 9]. The enhanced mechanical properties are largely due to precipitation strengthening, in which plate-like precipitates with habit planes perpendicular to the basal plane form during aging [3, 10, 11].

Understanding the mechanisms that govern the formation and growth of precipitates is crucial for designing Mg-RE alloys with tailored thermomechanical properties. Notably, among the RE elements, neodymium (Nd) exhibits the most pronounced age hardening when alloyed with Mg. This is primarily attributed to the high solid solubility of Nd in Mg, which allows for a high concentration of Nd during solution treatment [12, 13] and the subsequent formation of fine precipitate phases (e.g., Mg₃Nd) during aging, leading to a significant increase in hardness and strength. Consequently, Mg-Nd and Mg-Y-Nd alloys (with Y representing yttrium), which benefit from conventional age-hardening processes, are extensively used in aerospace and transportation applications [14, 15].

Experimental and computational studies have been conducted to investigate the phases, morphologies, and spatial arrangements of precipitates formed during the aging of Mg-Nd alloys. Natarajan et al. [8] performed a combined first-principles and experimental study to elucidate the precipitation sequence in binary Mg-Nd alloys. This sequence typically proceeds from a supersaturated solid solution (SSSS) to Guinier-Preston (GP) zones, followed by the precipitate phases β''' , β_1 , β , and β_c in that order. Ji et al. [16] utilized first-principles calculations and phase-field simulations to predict β' precipitate morphology. Liu et al. [17] used phase-field modeling to investigate the morphology of β_1 precipitates in Mg-Nd alloys. DeWitt et al. [18] examined the composition and morphology of coherent β''' precipitates, comparing predictions from three-dimensional (3D) phase-field simulations with high-angle annular dark field (HAADF) scanning

transmission electron microscopy (STEM) measurements. Zhu et al. [19] employed atomic-resolution HAADF-STEM to identify impinged β_1 variants in a characteristic triadic configuration.

While most studies have provided significant insights into the phases, morphologies, and spatial arrangements of precipitates in Mg–Nd alloys, less attention has been given to the evolution of precipitate populations across the stages of nucleation, growth, and coarsening. Coarsening is the process in which larger precipitates grow at the expense of smaller ones, driven by the reduction of interfacial energy [20, 21]. Understanding how precipitate number density changes during aging helps in choosing optimal time and temperature conditions to achieve a precipitate number density that results in the desired mechanical properties in Mg–Nd alloys. However, in many phase-field modeling studies, including but not limited to Mg–Nd systems, the evolution of precipitate number density across all aging stages is rarely examined. For example, Yang et al. [22] employed a phase-field model to investigate the effect of alloy composition on the evolution of precipitate number density, but they did not consider the coarsening stage. Liu et al. [23] focused on how number density affects alloy strengthening, without tracking its evolution across all aging stages. Ji et al. [24] examined morphological changes and interactions among precipitates rather than changes in precipitate number density.

A challenge in comparing the precipitate number densities from phase-field simulations and experimental characterization, e.g., transmission electron microscopy (TEM), is that experimental measurements are typically obtained from two-dimensional (2D) cross-sections, which may not accurately reflect the number density within the full 3D microstructure. On the simulation side, while 3D phase-field simulations provide a more realistic representation of the microstructure, simulating a statistically representative 3D sample often requires a significant amount of computational resources in general. For systems like Mg–Nd alloys, the demand for computational resources is especially high because the precipitates exhibit strong anisotropy and a high spatial resolution is required to accurately describe their morphology. Therefore, performing 2D phase-field simulations is often a practical choice. However, this approach requires careful stereological conversion strategies to parameterize the model, so that the number density evolution observed in 2D simulations represents the 3D evolution as closely as possible.

In this work, an integrated experimental and phase-field workflow was developed to model the evolution of β_1 precipitates in Mg–Nd alloys during aging, which involves nucleation, growth, and coarsening. Our proposed workflow involves extracting 3D precipitate number densities from 2D

experimental images and using these data to obtain input parameters for 2D phase-field simulations. The phase-field model implementation includes a stochastic method to introduce nuclei throughout the simulation. The model was parameterized using a combination of available literature data and experimental measurements, including matrix composition obtained via atom probe tomography (APT) and number density extracted from TEM images at various aging times. A validated model through this approach enables the prediction of process-structure relationships that allow for the optimization of aging conditions to achieve desired microstructures.

This paper is organized as follows. Section 2 describes the experimental procedures for measuring precipitate number density and average matrix composition at different aging times. Section 3 presents the simulation methods. Section 4 presents the results, including the experimental measurements, the model parameterization workflow and outcomes, the simulation results, and the comparison between the simulation and experimental results. We find that the parameterized model is capable of capturing the salient features of nucleation, growth, and coarsening behaviors observed in experiments. Section 5 summarizes the main conclusions of this work.

2. Experimental methods

2.1. Sample preparation

As-cast Mg–2.4 wt.% Nd billets, purchased from CanmetMATERIALS, Canada, were used in this study. The purchased billets were melted by resistance heating in a steel crucible, under a protective gas mixture of CO₂ and 0.5% SF₆ in an electric furnace, which was then poured into a mold to form ingots with a diameter of 3.5 inches. To produce β_1 precipitates, the cast alloy was first homogenized at 803 K for 3 h. The homogenized material was rapidly quenched in water and subsequently aged at 523 K to facilitate the precipitation of β_1 phase in Mg–Nd alloy. Further details regarding the casting, homogenization, quenching, and aging procedures can be found in Refs. [25, 26]. A total of five aging times were investigated: 3 h, 3.25 h, 4 h, 6 h, and 9 h at 523 K.

2.2. Determination of precipitate number density

TEM specimens were mechanically thinned to 100 μm and electropolished using a twin-jet polisher. High-resolution TEM images were obtained with a double aberration-corrected JEOL 3100R05 TEM operated at 300 kV. More details of this procedure can be found in Refs. [25, 26]. The TEM images acquired at different aging times were analyzed to determine the number densities of β_1 precipitates. However, the number of precipitates obtained by direct counting in a TEM image corresponds only to those present within the thin foil. Therefore, the precipitate count in the TEM image cannot be used to directly calculate the number density in the bulk material. To estimate the 3D number densities of precipitates from these 2D TEM images, a stereological correction was necessary. Several stereological methods have been reported for converting 2D measurements obtained from thin sections to 3D number densities, and these often require knowledge of the particle size distribution [27, 28]. Since the precipitate size distribution was not known in our case, we adopted the correction method described by Sonderegger [29], which does not rely on knowledge of the precipitate size distribution. Although this method was originally developed for spherical particles, it is straightforward to show that it can also be applied to plate-shaped particles with a circular cross-section perpendicular to the imaging plane.

2.3. Determination of matrix composition via APT

The matrix composition at different aging times was quantified via APT. Focused ion beam (FIB) lift-out was performed on a FEI Helios 650 dual-beam system to prepare needle-shaped APT specimens. A Cameca LEAP 5000XR instrument, operated in laser-pulsing mode with a pulse energy of 40–60 pJ and a specimen temperature of 30 K at a detection rate of 1.0 %, was used for the APT data acquisition. Data visualization and analysis were performed using the Integrated Visualization and Analysis Software (IVAS[®]) package. 3D tomographic reconstruction was performed with the radius evolution at shank mode, in which the shank angle was estimated from the high-resolution scanning electron microscopy (SEM) imaging on the APT needles. The following parameters were employed: voxel size = $1 \times 1 \times 1 \text{ nm}^3$, delocalization distance = 3 nm, and sample count threshold = 1 %.

3. Simulation methods

3.1. Phase-field model

During the transformation from the α -Mg phase with a hexagonal close-packed (hcp) structure to the β_1 phase with a face-centered cubic (fcc) ordering, which involves deformation and rigid body rotation, the symmetries of the α -Mg and β_1 lattices allow for three possible deformation variants [15]. Each of these has two orientation variants [15], generated by rotating the deformed lattice clockwise or counterclockwise by 5.3° . Rotating in either direction by the same angle yields the same stress-free transformation strain (SFTS) for a given deformation variant. Therefore, in the phase-field model, three order parameters η_1 , η_2 and η_3 are used to describe the three deformation variants. A given deformation variant, p , is represented by $\eta_p = 1$ and $\eta_{q \neq p} = 0$, where $p, q = 1, 2, 3$. The hcp α -Mg matrix phase is represented by $\eta_1 = \eta_2 = \eta_3 = 0$. For the same deformation variant, the two possible orientation variants result in two distinct habit planes for the β_1 precipitates. This leads to two primary growth directions of the precipitates described by the same order parameter in the phase-field model.

An additional variable, x_{Nd} , is used in the phase-field model to represent the Nd composition in mole fraction. In this work, we employed the Kim–Kim–Suzuki (KKS) model [17, 30], following the specific formulation by DeWitt et al. [18]. The total free energy functional is expressed as

$$F_{tot} = \int [f_{bulk}(x_{Nd}, \eta_1, \eta_2, \eta_3) + f_{grad}(\nabla \eta_1, \nabla \eta_2, \nabla \eta_3) + f_{el}(\eta_1, \eta_2, \eta_3, \mathbf{u})] dV, \quad (1)$$

where $f_{bulk}(x_{Nd}, \eta_1, \eta_2, \eta_3)$ represents the bulk free energy density, $f_{grad}(\nabla \eta_1, \nabla \eta_2, \nabla \eta_3)$ represents the gradient energy density, and $f_{el}(x_{Nd}, \eta_1, \eta_2, \eta_3, \mathbf{u})$ is the elastic strain energy density. The dependence of the elastic strain density on the displacement vector, \mathbf{u} , will be discussed later in the text.

The bulk free energy density, which is a function of the composition and three order parameters, is expressed as [18]

$$\begin{aligned}
f_{bulk}(x_{Nd}, \eta_1, \eta_2, \eta_3) &= f_{\alpha}(x_{Nd}^{\alpha}) \cdot \left(1 - \sum_{p=1}^3 H(\eta_p)\right) + f_{\beta_1}(x_{Nd}^{\beta_1}) \cdot \sum_{p=1}^3 H(\eta_p) \\
&+ f_{barrier}(\eta_1, \eta_2, \eta_3).
\end{aligned} \tag{2}$$

Here, x_{Nd}^{α} and $x_{Nd}^{\beta_1}$ are the auxiliary Nd compositions for the α -Mg and β_1 phases in the KKS model, respectively, and $f_{\alpha}(x_{Nd}^{\alpha})$ and $f_{\beta_1}(x_{Nd}^{\beta_1})$ are the chemical free energy densities of α -Mg and β_1 phases, respectively. The constraint $x_{Nd} + x_{Mg} = 1$ is assumed for each phase, where x_{Mg} is the composition of Mg. The polynomial $H(\eta_p) = \eta_p^3 (10 - 15\eta_p + 6\eta_p^2)$ interpolates the bulk free energy densities between the α -Mg and β_1 phases. The term $f_{barrier}(\eta_1, \eta_2, \eta_3)$, defined below, contributes to the precipitate-matrix interfacial energy and penalizes overlaps of different deformation variants.

Polynomial forms of $f_{\alpha}(x_{Nd}^{\alpha})$ and $f_{\beta_1}(x_{Nd}^{\beta_1})$ are used in this model, as described in Ref. [18]:

$$f_{\alpha}(x_{Nd}^{\alpha}) = A_0 + A_1 x_{Nd}^{\alpha} + A_2 (x_{Nd}^{\alpha})^2, \tag{3}$$

$$f_{\beta_1}(x_{Nd}^{\beta_1}) = B_0 + B_1 x_{Nd}^{\beta_1} + B_2 (x_{Nd}^{\beta_1})^2. \tag{4}$$

Here, A_0, A_1, A_2, B_0, B_1 and B_2 are constants defining the chemical free energy density functions. These constants were obtained by performing quadratic fits to the chemical free energy densities calculated using the CALPHAD (CALculation of PHase Diagrams) method near equilibrium compositions. The auxiliary compositions, x_{Nd}^{α} and $x_{Nd}^{\beta_1}$, are given by [18]

$$x_{Nd}^{\alpha}(x_{Nd}, \eta_1, \eta_2, \eta_3) = \frac{B_2 x_{Nd} + \frac{1}{2}(B_1 - A_1) \sum_{p=1}^3 H(\eta_p)}{A_2 \sum_{p=1}^3 H(\eta_p) + B_2 [1 - \sum_{p=1}^3 H(\eta_p)]}, \tag{5}$$

and

$$x_{Nd}^{\beta_1}(x_{Nd}, \eta_1, \eta_2, \eta_3) = \frac{A_2 x_{Nd} + \frac{1}{2}(A_1 - B_1) [1 - \sum_{p=1}^3 H(\eta_p)]}{A_2 \sum_{p=1}^3 H(\eta_p) + B_2 [1 - \sum_{p=1}^3 H(\eta_p)]}. \tag{6}$$

The energy barrier term is [18]

$$\begin{aligned}
f_{barrier}(\eta_1, \eta_2, \eta_3) &= W[(\eta_1^2 + \eta_2^2 + \eta_3^2) - 2(\eta_1^3 + \eta_2^3 + \eta_3^3) + (\eta_1^4 + \eta_2^4 + \eta_3^4) \\
&+ 5(\eta_1^2 \eta_2^2 + \eta_2^2 \eta_3^2 + \eta_1^2 \eta_3^2) + 5\eta_1^2 \eta_2^2 \eta_3^2],
\end{aligned} \tag{7}$$

where W is the constant that controls the barrier heights between deformation variants.

The gradient energy density term, which depends on the gradients of the order parameters, takes the form [18]

$$f_{grad}(\nabla\eta_1, \nabla\eta_2, \nabla\eta_3) = \frac{1}{2} \sum_{p=1}^3 \kappa_{ij}^p \left(\frac{\partial\eta_p}{\partial r_i} \right) \left(\frac{\partial\eta_p}{\partial r_j} \right), \quad (8)$$

where the index, p , represents each variant, and κ_{ij}^p is the gradient energy coefficient tensor element for the order parameter, η_p , and the variables r_i and r_j represent the Cartesian coordinates with i and j as the spatial indices. The Einstein summation notation is used for the spatial indices, in which the sum over repeated indices is implied.

Based on Eshelby's theory of inclusions [31], the elastic strain energy term expressed in terms of the order parameters proposed by Khachaturyan [32] is given by

$$\begin{aligned} f_{el}(\eta_1, \eta_2, \eta_3, \mathbf{u}) \\ = \frac{1}{2} C_{ijkl}(\eta_1, \eta_2, \eta_3) [\epsilon_{ij}(\mathbf{u}) - \epsilon_{ij}^0(\eta_1, \eta_2, \eta_3)] [\epsilon_{kl}(\mathbf{u}) \\ - \epsilon_{kl}^0(\eta_1, \eta_2, \eta_3)], \end{aligned} \quad (9)$$

where C_{ijkl} denotes an element of the stiffness tensor and ϵ_{ij} is an element of the strain tensor, which depends on the displacement vector, \mathbf{u} . The terms ϵ_{ij}^0 are elements in SFTS. We ignore the concentration dependence of elastic properties within each phase since the precipitate is an intermetallic and the Nd concentration in the matrix is very low ($\leq 0.4\%$). The stiffness tensor and SFTS are interpolated between the matrix and precipitate values via [18]

$$\mathbf{C}(\eta_1, \eta_2, \eta_3) = \sum_{p=1}^3 \mathbf{C}^{\eta_p} H(\eta_p) + \mathbf{C}^\alpha \left[1 - \sum_{p=1}^3 H(\eta_p) \right], \quad (10)$$

$$\boldsymbol{\epsilon}^0(\eta_1, \eta_2, \eta_3) = \sum_{p=1}^3 \boldsymbol{\epsilon}^{\eta_p} H(\eta_p) + \boldsymbol{\epsilon}^\alpha \left[1 - \sum_{p=1}^3 H(\eta_p) \right], \quad (11)$$

where \mathbf{C}^{η_p} is the stiffness tensor for the p^{th} variant, \mathbf{C}^α is the stiffness tensor for the α -Mg matrix, $\boldsymbol{\epsilon}^{\eta_p}$ is the SFTS for the p^{th} variant, and $\boldsymbol{\epsilon}^\alpha$ is the SFTS for the α -Mg matrix. The elastic strain tensor, defined in terms of the displacement vector, \mathbf{u} , is written as [18]

$$\epsilon_{ij}(\mathbf{u}) = \frac{1}{2} \left(\frac{\partial u_j}{\partial r_i} + \frac{\partial u_i}{\partial r_j} \right). \quad (12)$$

The mechanical equilibrium condition

$$\frac{\partial}{\partial r_j} (C_{ijkl}(\eta_1, \eta_2, \eta_3) [\epsilon_{kl}(\mathbf{u}) - \epsilon_{kl}^0(\eta_1, \eta_2, \eta_3)]) = 0 \quad (13)$$

is solved to determine \mathbf{u} , which is used in the evolution equation, given below.

The Cahn–Hilliard [33] and Allen–Cahn [34] equations, which contain the variational derivatives of F_{tot} with respect to x_{Nd} and η_p , respectively, are used to describe the temporal evolution of the composition and structural order parameter fields [18]:

$$\begin{aligned} \frac{\partial x_{Nd}}{\partial t} = D \nabla \cdot \left\{ \nabla x_{Nd} + (x_{Nd}^\alpha - x_{Nd}^{\beta_1}) \sum_{p=1}^3 \left[\frac{\partial H(\eta_p)}{\partial \eta_p} \nabla \eta_p \right] \right. \\ \left. - \left(\frac{\partial^2 f_{bulk}}{\partial x_{Nd}^2} \right)^{-1} \nabla \left[C_{ijkl} \left(\frac{\partial \epsilon_{ij}^0}{\partial x_{Nd}} \right) (\epsilon_{kl} - \epsilon_{kl}^0) \right] \right\}, \end{aligned} \quad (14)$$

$$\begin{aligned} \frac{\partial \eta_p}{\partial t} = -L \left\{ \left[f_{\beta_1} - f_\alpha - (x_{Nd}^\alpha - x_{Nd}^{\beta_1}) \frac{\partial f_{\beta_1}}{\partial x_{Nd}^{\beta_1}} \right] \frac{\partial H(\eta_p)}{\partial \eta_p} + \frac{\partial f_{barrier}}{\partial \eta_p} \right. \\ \left. - \kappa_{ij}^p \frac{\partial^2 \eta_p}{\partial r_i \partial r_j} - C_{ijkl} \left(\frac{\partial \epsilon_{ij}^0}{\partial \eta_p} \right) (\epsilon_{kl} - \epsilon_{kl}^0) \right. \\ \left. + \frac{1}{2} \frac{\partial C_{ijkl}}{\partial \eta_p} (\epsilon_{ij} - \epsilon_{ij}^0) (\epsilon_{kl} - \epsilon_{kl}^0) \right\}, \end{aligned} \quad (15)$$

where D is the diffusion coefficient and L is the kinetic interface mobility; both are assumed constant and isotropic in this model for simplicity.

The phase-field model in this study was parameterized by selecting thermodynamic, elastic, and kinetic parameters to capture the evolution of β_1 precipitates in the Mg–Nd alloy at 523 K, as will be discussed in section 4.3. All parameters were converted into nondimensional units for simulations using characteristic scales for energy, length, and time. Further details will be provided in section 3.3.

3.2. Nucleus seeding method

To simulate concurrent precipitate nucleation and growth, a stochastic method to introduce nuclei was coupled with the phase-field model. We employ the method proposed by Jokisaari et al. [35] that extended the approach by Simmons et al. [36]. According to the classical nucleation theory,

the nucleation rate, $J(\mathbf{r}, t)$, defined as the number of new nuclei formed per unit volume per unit time at the spatial position \mathbf{r} and time t , is given by [37]

$$J(\mathbf{r}, t) = ZN_n\beta \exp\left(-\frac{\Delta G^*}{kT}\right) \exp\left(-\frac{\tau_{in}}{t}\right), \quad (16)$$

where Z is the Zeldovich factor, N_n is the number of nucleation sites per unit volume, β is the frequency of molecular attachment to the nucleus, ΔG^* is the nucleation energy barrier, k is the Boltzmann constant, T is the temperature, and τ_{in} is the incubation time. For a spherical nucleus in 3D, the nucleation energy barrier is expressed as [37]

$$\Delta G^* = \frac{16\pi\gamma^3}{3(\Delta G_v - \Delta G_{strain})^2}, \quad (17)$$

where γ is the interfacial energy between the matrix and precipitate phases, ΔG_v is the bulk free energy change during nucleation per the unit volume of the nucleus, and ΔG_{strain} is the misfit strain energy per the unit volume of the nucleus. As described in the SI, we numerically calculated a posteriori the ratio $|\Delta G_{strain}|/|\Delta G_v|$ of an isolated seed. We found this ratio to be less than 1/10 initially, when the supersaturation is maximum, but becomes as large as 1/2 at the ending stage of nucleation when supersaturation decreases. Nevertheless, we neglect ΔG_{strain} in equation (16) since self-consistently computing it is challenging due to the long-range nature of elastic interactions.

We also show in the SI that ΔG_v is approximately proportional to $\Delta x(\mathbf{r}, t)$ and, when ignoring ΔG_{strain} , the nucleation rate can be written as [36]

$$J(\mathbf{r}, t) = \rho_1 \exp\left(-\frac{\rho_2}{[\Delta x(\mathbf{r}, t)]^2}\right) \exp\left(-\frac{\tau_{in}}{t}\right), \quad (18)$$

where ρ_1 and ρ_2 are combinations of physical constants (further discussed in section 4.4) and the dimensionality in equation (18) is assumed to be 3. We preserve the form $\exp(-\rho_2/\Delta x^2)$ in our seeding method, even though the simulations are carried out in 2D, to preserve the same dependence of nucleation rate on supersaturation as in a 3D system. The supersaturation, $\Delta x(\mathbf{r}, t)$, at position, \mathbf{r} , and time, t , is defined as

$$\Delta x(\mathbf{r}, t) = x(\mathbf{r}, t) - x_e^\alpha, \quad (19)$$

where $x(\mathbf{r}, t)$ is the local matrix composition and x_e^α is the equilibrium matrix composition. With the assumption that J is uniform within a small volume ΔV and constant during a small time

interval Δt_{nuc} , the local probability, $P(\mathbf{r}, t)$, that at least one nucleation event can occur in ΔV within Δt_{nuc} can be expressed as [35, 36]

$$P(\mathbf{r}, t) = 1 - \exp(-J\Delta V\Delta t_{nuc}). \quad (20)$$

The nucleation probability, which varies spatially with local supersaturation and changes over time, is evaluated for every element of the mesh in the computational domain at fixed time intervals. A nucleus is introduced within the element whenever this probability exceeds a random number drawn from a uniform distribution in the interval (0,1). During the simulation, insertion of a nucleus is accomplished by modifying the order parameter corresponding to a randomly chosen deformation variant of the precipitate phase. This modification is applied within a small elliptical region centered on the nucleation site, with its major axis along one of the two possible orientations of the selected deformation variant, which is also chosen at random. A short holding period is imposed after seeding the nucleus [35]. During the holding period, the structural order parameter near the nucleation site is maintained, thereby preserving the driving force for initial solute accumulation and preventing the immediate dissolution of the newly formed nucleus.

While this nucleus seeding algorithm provides a stochastic method for introducing nuclei that takes into account the local conditions, many of its parameters are not directly obtainable or have significant uncertainties such as the Zeldovich factor, molecular attachment frequency, geometric factor (in the case of heterogeneous nucleation), interfacial energy (which appears with third power), equilibrium compositions in each phase, and supersaturation as a function of time and space. Thus, we employ a multistep parameterization procedure, which is summarized below and described in detail in section 4.4. Experimental TEM images were processed to estimate 3D number densities, which were then converted from 3D to 2D for use in 2D simulations, by maintaining the same characteristic interparticle distances. Initial optimization of nucleation rate parameters was performed to minimize discrepancies between the experimental number densities and the model that assumes uniform supersaturation. The simulation was then conducted with this set of parameters. To correct for the limitations inherent in the uniform-supersaturation model, the simulation time scale is adjusted, which is equivalent to scaling ρ_1 , D , and τ_{in}^{-1} with the same factor, by optimizing the match between the corrected simulation results and experimental data. This workflow ensures that the modeling framework is robustly calibrated to physical realities while maintaining computational efficiency. It is important to note that we ignore the intermediate phases that are involved in the formation of β_1 precipitates. This approximation allows us to

employ a simplified model that considers a single effective nucleation barrier and to avoid tracking the populations of intermediate precipitate phases, which would introduce additional model parameters and increase computational cost. Thus, the nucleation parameters determined in this work are effective, empirical values that represent the rate-limiting step.

3.3. Numerical implementation

The governing equations (equations (13)–(15)) were nondimensionalized and implemented in PRISMS-PF [38], an open-source high-performance phase-field framework, using an unstructured mesh with quadrilateral second-order elements. The characteristic energy density, $f^* = 2 \times 10^9 \text{ J/m}^3 = 2 \times 10^{-18} \text{ J/nm}^3$, and the characteristic length, $l^* = 10^{-9} \text{ m} = 1 \text{ nm}$, were used for nondimensionalization. The dimensionless diffusivity was chosen to be 1, which sets the time scale to be $t^* = l^{*2}/D$; D is determined in the parameterization process described in section 4.4. All simulations were performed in a square domain with a side length of $1100l^*$. The side length of square-shaped elements ranges from $1100l^*/2^{12}$ to $1100l^*/2^6$, which varies based on the adaptive-mesh-refinement conditions. The interfacial width was resolved by approximately 5.6 second-order elements. The time step was chosen to be $2.5 \times 10^{-3}t^*$, which yielded numerical stability. A nucleus seeding attempt was made every $2.5t^*$, which gives Δt_{nuc} in equation (20); this value is much smaller than the characteristic time scale for nucleation at the peak rate (on the order of 10^3t^*). The seed has semi-major and semi-minor axis lengths of $3l^*$ and $2l^*$, respectively. The holding period after seeding a nucleus was set to $100t^*$, which was found to be sufficient to stabilize a seed. A solid solution of uniform Nd composition of 0.004 in mole fraction was set as the initial condition, and periodic boundary conditions were employed.

4. Results and discussions

4.1. Determination of precipitate number density

This study focuses specifically on β_1 precipitates in Mg–Nd alloys within the precipitation sequence [8]: SSSS \rightarrow GP zones \rightarrow β''' precipitates (a hybrid ordering of β' with a Mg_7Nd composition and β'' with a Mg_3Nd composition) \rightarrow β_1 precipitates (Mg_3Nd) \rightarrow β precipitates (Mg_{12}Nd) \rightarrow β_e precipitates (Mg_{41}Nd). The last two phases were not observed under the

experimental condition we investigated. The β_1 precipitates exhibit a plate-like morphology, with a habit plane of $\{1\bar{1}00\}_\alpha$ in the matrix. The orientation relationship between the β_1 precipitates and the α -Mg matrix is $\{\bar{1}12\}_{\beta_1} // \{1\bar{1}00\}_\alpha$ and $\langle 110 \rangle_{\beta_1} // [0001]_\alpha$ [15]. The morphologies and spatial distributions of β_1 precipitates at various aging times are shown in figure 1.

The estimated 3D number density for each sample was calculated from the measured length along the precipitate's major axis in a TEM image, $d_{m,i}$, where i indexes the precipitates. The measurements were made using ImageJ [39] by manually overlaying each precipitate with an ellipse with similar dimensions. The estimated 3D number density from each TEM image was obtained by using [29]

$$N_v^{exp} = \frac{1}{A_{sample}} \sum_{i=1}^N \frac{1}{t_{foil} + d_{m,i}}, \quad (21)$$

where t_{foil} is the foil thickness, and A_{sample} is the sample area. Table 1 summarizes the measured sample area, foil thickness, and the corresponding estimated 3D number density for each TEM image shown in figure 1.

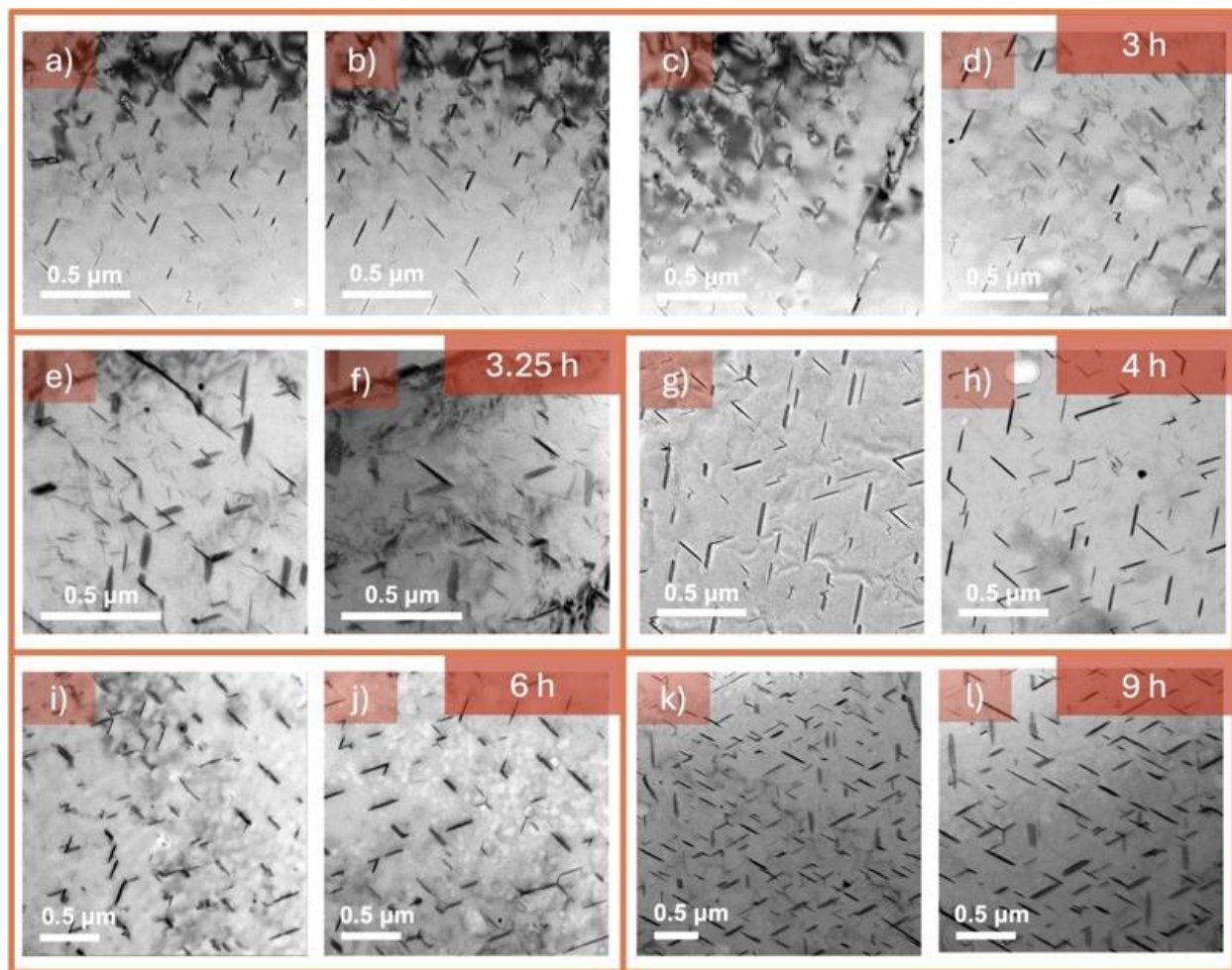


Figure 1. TEM images showing the microstructures of β_1 precipitates in Mg–Nd alloys at various aging times: (a–d) 3 h, (e–f) 3.25 h, (g–h) 4 h, (i–j) 6 h, and (k–l) 9 h, all at 523 K. All foils were oriented along the $[0001]$ direction of the α -Mg matrix. Note that the scale bars vary in size across the subfigures.

Table 1. Measured sample area, foil thickness, and estimated 3D number density for each TEM image in figure 1.

Figure 1 panel	Aging time t (h)	Sample area A_{sample} (μm^2)	Foil thickness t_{foil} (μm)	3D number density N_v^{exp} (count/μm^3)
(a)	3	2.56	0.158	87.9
(b)	3	2.56	0.158	83.8
(c)	3	2.56	0.158	82.0
(d)	3	2.56	0.158	81.2
(e)	3.25	1.40	0.224	125.6
(f)	3.25	1.40	0.224	115.4
(g)	4	2.56	0.182	162.6
(h)	4	2.56	0.182	158.5
(i)	6	5.82	0.141	79.6
(j)	6	5.82	0.141	78.0
(k)	9	10.19	0.377	64.1
(l)	9	5.83	0.377	69.3

4.2. Determination of matrix composition

To further elucidate the microstructural evolution during aging, the composition of the matrix was assessed using APT. Composition measurements of the alloying element were obtained across the

matrix/precipitate interface with a bin size of 0.5 nm for three different aging times: 4 h, 6 h, and 100 h. APT datasets were acquired and analyzed from 2 to 4 APT specimens for each aging time. The matrix compositions were determined by analyzing matrix regions located sufficiently away from the interface. For dilute species detected via APT, such as Nd atoms in the matrix, the statistical uncertainty in the measured composition can be estimated using Poisson statistics [40, 41]

$$\sigma = \sqrt{\frac{x_{Nd}(1 - x_{Nd})}{T_{all}}}, \quad (22)$$

where σ is the statistical uncertainty in Nd composition, x_{Nd} is the measured Nd composition, and T_{all} is the total atom count. The APT measurements and corresponding statistical uncertainties are summarized in table 2. The data at 100 h are included in the table to demonstrate that, by 6 h, the matrix composition has approached the asymptotic limit, and they are not used in later parameterization or results. The Poisson uncertainty values, which represent the lower bounds for the measurement error, are one to two orders of magnitude smaller than the corresponding Nd mole fractions, highlighting the high precision of atom counting. However, the variations observed between repeated measurements in table 2 are larger than the statistical uncertainties. This implies substantial contributions from other sources of measurement uncertainty, such as systematic factors like detector efficiency, as well as actual spatial variations [42, 43].

Table 2. Summary of APT measurements of matrix Nd composition (expressed as mole fraction) and corresponding statistical uncertainties at different aging times.

Aging times	Measurement	Nd atoms / total atoms detected	Mole fraction of Nd (x_{Nd})	Statistical uncertainty (σ)
4 h	1	274/869046	3.15×10^{-4}	1.90×10^{-5}
	2	35/82308	4.25×10^{-4}	7.19×10^{-5}
	3	22/61318	3.59×10^{-4}	7.65×10^{-5}
	4	123/341201	3.60×10^{-4}	3.25×10^{-5}
6 h	1	4309/11530212	3.74×10^{-4}	5.69×10^{-6}
	2	66/223655	2.95×10^{-4}	3.63×10^{-5}
100 h	1	261/908410	2.87×10^{-4}	1.78×10^{-5}
	2	328/1598256	2.05×10^{-4}	1.13×10^{-5}
	3	1915/5190376	3.69×10^{-4}	8.43×10^{-6}

4.3. Phase-field model parameters

The chemical free energy densities of the α -Mg matrix and β_1 precipitate phases used in this work were obtained using the CALPHAD method. We surveyed several CALPHAD studies on the Mg–Nd system and found that the equilibrium compositions reported for the matrix and β_1 phases at 523 K vary across different thermodynamic databases, as summarized in table 3. The Mg–Nd thermodynamic database from Qi et al. [44] was selected for use in this study, as it yields simulated matrix compositions that are in closest agreement with our experimental APT measurements, specifically the asymptotic value of matrix composition at late aging times. The CALPHAD free energy curves for the α -Mg matrix and β_1 phases are presented in figure 2(a). Equivalent free

energy functions were obtained by subtracting the common tangent line from the original CALPHAD curves. As shown in figure 2(b), these adjusted free energies were fitted to quadratic functions around the equilibrium compositions. This fitting procedure ensures that the equilibrium concentrations are retained in the resulting fitted free energy densities. The coefficients obtained for the fitted parabolic functions in equations (3) and (4) are: $A_0 = 4.00 \times 10^{-1}$ J/mol, $A_1 = -4.23 \times 10^3$ J/mol, $A_2 = 1.12 \times 10^7$ J/mol, $B_0 = 1.71 \times 10^4$ J/mol, $B_1 = -1.41 \times 10^5$ J/mol, and $B_2 = 2.89 \times 10^5$ J/mol.

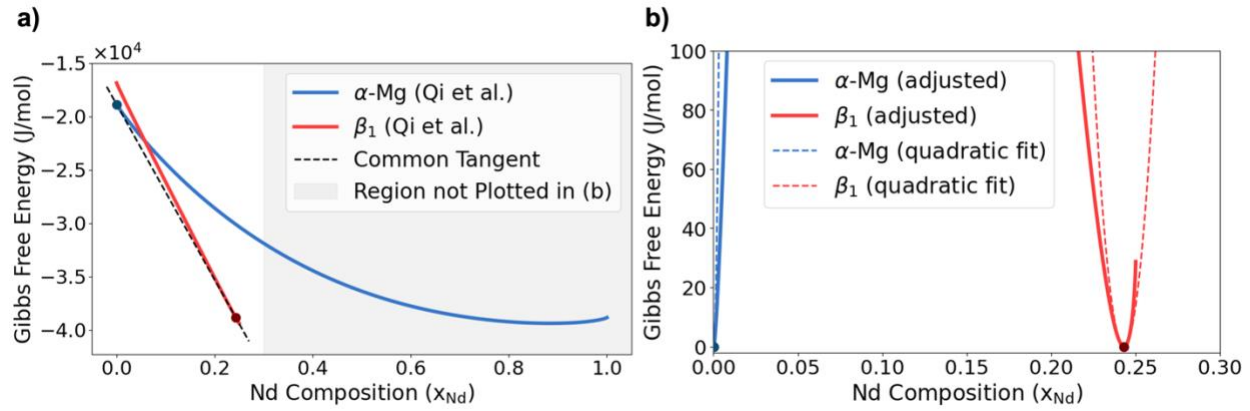


Figure 2. (a) Molar Gibbs free energy of the α -Mg matrix and β_1 phases plotted as a function of Nd composition at 523 K, calculated using the thermodynamic parameters from Qi et al. [44]. (b) Adjusted Gibbs free energy curves for the two phases, obtained by subtracting the common tangent from the original curves, with quadratic fits applied near the equilibrium compositions.

The interfacial energy between the β_1 and hcp α -Mg phases is assumed to be isotropic in this study for simplicity. Thus, we take $\kappa_{ij} = K\delta_{ij}$ in section 3.1, where δ_{ij} is the Kronecker delta and K is the gradient energy coefficient. An interfacial energy of $\gamma = 0.05$ J/m² was selected to maintain consistency with a previous phase-field study [17] due to the lack of experimental values in the literature. The interfacial energy in this model is related to the phase-field model parameters by [16, 30]

$$\gamma = \sqrt{KW}/(3\sqrt{2}), \quad (23)$$

where $K = 5.115 \times 10^{-2} f^*/l^{*2}$ and $W = 0.22f^*$ is the constant in the energy barrier term in equation (7). These constants were chosen to yield the desired γ , while setting an equilibrium interface width from $\eta_p = 0.1$ to 0.9 to be $\delta \approx 2.2\sqrt{2KW} = 1.5l^*$, which is resolved by

approximately 5.6 second-order elements, as mentioned in section 3.3. A diffusivity value of $D = 7.5 \times 10^{-18} \text{ m}^2/\text{s}$, which is similar to a value for Nd in pure Mg reported in Ref. [45], was adopted in the simulation before fine-tuning model parameters. The fine-tuning of the time scale required to optimize the agreement between the simulation and experiment was equivalent to using a diffusivity of $D = 10.4 \times 10^{-18} \text{ m}^2/\text{s}$, as discussed in section 4.4.

Table 3. Summary of equilibrium Nd compositions in the matrix phase and β_1 phase at 523 K obtained from different thermodynamic databases.

Mg–Nd system thermodynamic database	Equilibrium Nd mole fraction in the matrix at 523 K	Equilibrium Nd mole fraction in the β_1 precipitates at 523 K
Niu et al. 2010 [46]	1.00×10^{-14}	2.35×10^{-1}
Qi et al. 2011 [44]	1.89×10^{-4}	2.43×10^{-1}
Kang et al. 2012 [47]	1.56×10^{-4}	2.14×10^{-1}
Guo et al. 2013 [48]	7.20×10^{-5}	2.35×10^{-1}
Luo et al. 2025 [49]	3.56×10^{-4}	2.23×10^{-1}

The elastic constants of the β_1 precipitates are assumed to be identical to those of the α -Mg matrix phase, as in Ref. [17]. The following reported elastic constants for the matrix phase were used [16]: $C_{1111} = C_{2222} = 62.6 \text{ GPa}$, $C_{3333} = 64.9 \text{ GPa}$; $C_{1122} = 26.0 \text{ GPa}$; $C_{1133} = C_{2233} = 20.9 \text{ GPa}$; $C_{2323} = C_{1313} = 13.3 \text{ GPa}$; and $C_{1212} = 18.3 \text{ GPa}$. Following Refs. [16, 18], the SFTS of the α -Mg matrix phase is set to be $\epsilon^\alpha = 0$. The SFTSs of the precipitate phase were adopted from Ref. [17]:

$$\epsilon^{\eta_1} = \begin{bmatrix} 0.1111 & 0.0962 & 0 \\ 0.0962 & 0 & 0 \\ 0 & 0 & 0 \end{bmatrix}, \quad (24)$$

$$\epsilon^{\eta_2} = \begin{bmatrix} -0.0556 & 0 & 0 \\ 0 & 0.1666 & 0 \\ 0 & 0 & 0 \end{bmatrix}, \quad (25)$$

$$\epsilon^{\eta_3} = \begin{bmatrix} 0.1111 & -0.0962 & 0 \\ -0.0962 & 0 & 0 \\ 0 & 0 & 0 \end{bmatrix}, \quad (26)$$

where the SFTS in the out-of-plane direction is ignored.

4.4. Parameterization workflow

The model parameterization workflow involved the following steps, which are further detailed:

- 1) Obtain the effective 2D number density from the estimated 3D number density presented in section 4.1 to 2D for phase-field simulations.
- 2) Perform an initial optimization of parameters ρ_1 , ρ_2 and τ_{in} in equation (18), which determine the nucleation rate.
- 3) Find a diffusivity value that yields reasonable agreement between simulated and effective 2D number density evolution. Conduct the simulation using this diffusivity and the nucleation rate parameters found in step 2.
- 4) Fine-tune the simulation time scale by further optimizing the agreement between simulated and the effective 2D number density evolution.

Step 1. Obtain the effective 2D number density from the 3D number density

For computational efficiency, the phase-field simulations were performed in 2D rather than 3D. However, a key discrepancy exists between 2D and 3D spatial dimensions regarding particle interactions. To reconcile this, we applied a scheme to obtain the effective 2D number density from the estimated 3D number density data that preserves the characteristic interparticle distance over which diffusion must occur during coarsening. To establish the relationship, we assume a statistically uniform spatial distribution of precipitates and the same characteristic interparticle distance, λ , both in 2D and 3D. Therefore, the number density per unit volume in 3D, $N_v = \lambda^{-3}$, and the number density per unit area in 2D, $N_A = \lambda^{-2}$, can be related by

$$N_A = N_v^{2/3}. \quad (27)$$

We employ this relationship to obtain the effective 2D number densities for different aging times, $N_A^{eff}(t)$, to parameterize the phase-field model, as described in the following steps.

Step 2. Perform initial optimization of nucleation rate parameters

To quantitatively model nucleation behavior in this system, it is necessary to set the three parameters, ρ_1 , ρ_2 and τ_{in} , that determine the nucleation rate via equation (18). As mentioned earlier, these parameters cannot be uniquely determined directly from the available experimental data. However, an initial optimization can be performed by (1) selecting initial guesses for the values of ρ_1 , ρ_2 and τ_{in} within a set of bounds based on either models or experimental observations, (2) integrating the nucleation rate over time during the nucleation stage to calculate the number density, $N_A(t)$, and (3) optimizing ρ_1 , ρ_2 and τ_{in} to minimize the difference between $N_A(t)$ and $N_A^{eff}(t)$. For this initial optimization, we ignore the spatial variation in supersaturation and treat it as a function of time only. The limitations of this uniform-supersaturation model are addressed using the fine-tuning method discussed in step 4. The time dependence of supersaturation is accounted for by modeling the Nd composition in the matrix, x , as a function of aging time using a hyperbolic tangent function. This function captures how the supersaturation decreases rapidly during the nucleation stage and then transitions to the equilibrium value as it enters the coarsening stage. The APT measurements are used to set the initial and asymptotic values of the matrix composition (Table 2 and Figure S1(a)), while the transition time and width are estimated from the number density data measured from the micrograph (Table 1 and Figure S1(b)). The resulting function, $x_{fit}(t)$, is shown in figure S1(a) in the SI. From this function, the supersaturation, $\Delta x_{fit}(t) = x_{fit}(t) - x_e$, was obtained, where x_e is the asymptotic value of $x_{fit}(t)$ at late aging times. Then, the number density as a function of time can be estimated by

$$N_A(t) = \int_0^t J(\Delta x_{fit}(t'), t'; \rho_1, \rho_2, \tau,) dt'. \quad (28)$$

The search bounds for each nucleation rate parameter (listed in table 4) were determined as follows. In classical nucleation theory, the incubation time, τ_{in} , represents the characteristic time before the nucleation rate reaches steady state. As shown in figure 3(a), the experimental number density increases significantly between 2.0 h and 3.0 h. Therefore, a search range from 0.0 to 3.0 h was established for finding the optimal value of τ_{in} . The optimization yielded an incubation time

at the upper bound of the allowed interval (approximately 3.0 h). When a broader interval (0.0–10.0 h) was chosen for the optimization, the best-fit value shifted to approximately 6.9 h. However, this value provided only a minor improvement to the fit and is inconsistent with the assumption that the time to reach steady-state nucleation is determined by τ_{in} . Therefore, $\tau_{in} = 3.0$ h was used as the incubation time.

For ρ_2 , we used an approximate value given by

$$\rho_2 = \frac{4\pi\gamma^3 V_m^2}{3kT(A_2)^2(x_e^{\beta_1} - x_e^\alpha)^2}, \quad (29)$$

where V_m is the molar volume, and x_e^α and $x_e^{\beta_1}$ are the equilibrium Nd compositions in the matrix and β_1 phases, respectively. The derivation for this expression follows a similar approach to that of Ref. [50], and is presented in the SI. The value of ρ_2 depends on several physical parameters, each with an associated uncertainty. For x_e^α and $x_e^{\beta_1}$, ranges of 1×10^{-5} – 5×10^{-4} and 0.2–0.25, respectively, were chosen based on the survey summarized in table 3. For γ , only two values were found in the literature: 0.098 J/m² reported from DFT calculations [51], and 0.05 J/m² used in Ref. [17]. Considering the two γ values and the ranges for $x_e^{\beta_1}$ and for x_e^α , the calculated ρ_2 falls within a range between 2.84×10^{-6} and 1.45×10^{-5} . Given that the range of ρ_2 corresponding to these γ values spans more than one order of magnitude, this demonstrates pronounced sensitivity of ρ_2 to the value of γ . To ensure that the optimization process can adequately explore this uncertainty, the lower and upper bounds of ρ_2 were expanded to 1.0×10^{-7} and 1.0×10^{-4} , respectively. This broader optimization range minimizes the risk of artificially constraining the parameter space and thereby enables more robust identification of optimal values.

The optimization bounds for ρ_1 were established starting from an order-of-magnitude estimate of the steady-state nucleation rate, J_{ss} , assuming it was achieved in the experiment, and expanding the range from that value. According to equation (18), in the limit $t \gg \tau$, $J_{ss} \approx \rho_1 \exp[-\rho_2(\Delta x)^{-2}]$. If the supersaturation, Δx , is sufficiently large (such that $\Delta x^2 \gg \rho_2$), the exponential term $\exp[-\rho_2(\Delta x)^{-2}]$ approaches unity, so $J_{ss} \approx \rho_1$. As shown by the experimental data in figure 3(a), the number density increases by approximately 10^{13} m^{-2} between 2.0 h and 3.0 h of aging, giving $J_{ss} \approx 10^{13} \text{ m}^{-2}\text{h}^{-1}$ to the order of magnitude (see Figure S1(b)). Given the uncertainty in this approximation, the optimization bounds for ρ_1 were chosen to span two orders of magnitude above and below $10^{13} \text{ m}^{-2}\text{h}^{-1}$.

Global optimization was performed within these bounds using the differential evolution algorithm [52] from the Python package SciPy [53]. The effective 2D number density starts to decrease after 4.0 h, which is taken as the onset of the coarsening stage. Therefore, only data points before this time were used for nucleation rate parameter optimization. The resulting optimized nucleation rate parameters of this initial step are listed in table 4. Using these parameters, the evolution of number density calculated from the classical nucleation theory is plotted as the orange curve in figure 3(a).

Table 4. Nucleation rate parameter bounds used in parameter optimization and resulting optimized values.

Nucleation rate parameter	ρ_1 ($\text{m}^{-2}\text{h}^{-1}$)	ρ_2	τ_{in} (h)
Optimization bound	$[10^{11}, 10^{15}]$	$[1.0 \times 10^{-7}, 1.0 \times 10^{-4}]$	$[0.0, 3.0]$
Optimized value	4.61×10^{13}	1.74×10^{-7}	3.0

Step 3. Obtain an estimated value of diffusivity

We started with a reported diffusivity coefficient for Nd atoms in the pure hcp-Mg phase, which is approximately $7.0 \times 10^{-18} \text{ m}^2/\text{s}$ at 523 K [45]. In the absence of precise experimental or theoretical data for Nd diffusivity in the hcp α -Mg matrix phase at 523 K, we conducted exploratory phase-field simulations based on this diffusivity value. Using the initially optimized nucleation rate parameters, we tested three additional diffusivity values: $6.5 \times 10^{-18} \text{ m}^2/\text{s}$, $7.5 \times 10^{-18} \text{ m}^2/\text{s}$, and $8.0 \times 10^{-18} \text{ m}^2/\text{s}$. Out of these simulations, that with $7.5 \times 10^{-18} \text{ m}^2/\text{s}$ yielded the best agreement with the effective 2D number densities converted from the 3D experimental values, specifically the maximum number density and the rate of decrease in the number density during the coarsening stage. Thus, the result from this simulation was used for the fine-tuning step below. Despite our exploration in diffusivity values, the predicted number density

shows a noticeable discrepancy from the simulated results (green curve in figure 3(a)). As discussed below, this discrepancy can be further reduced by fine-tuning the model parameters.

Step 4. Fine-tune the model parameters

Recognizing the limitations in the initial optimization of nucleation parameters based on the uniform-supersaturation model, a method is proposed to correct model parameters. By observing that the change in the time scale significantly improves the agreement between the experimental data and the simulation prediction obtained, we determine a correction factor (CF) to the time scale. This is equivalent to adjusting the model parameters such that $\rho_1' = \rho_1 \cdot CF$, $\tau_{in}' = \tau_{in}/CF$ and $D' = D \cdot CF$. During the nucleation stage, both the parameterized nucleation rate and the diffusivity affect the rate of change in number density. The optimal value of CF was determined by minimizing an error metric defined as the integrated absolute differences between the trial number density curves (calculated using various CF values) and predicted number density curve during the nucleation and growth stages (defined as 0 to 4 hours). As shown in figure 3(b), a third-order polynomial was fitted to the plot of error vs. CF to identify the minimum error, which was found at $CF = 1.39$, as shown in figure 3(b). To ensure statistical reliability, two additional independent simulations, besides the one shown in figure 3, were conducted using the same initially optimized nucleation rate parameters and analyzed in the same way to obtain their optimal CF values. The three independent simulations yielded optimal CF values of 1.39, 1.46, and 1.39, with a mean of 1.41 and a low standard deviation of 0.033, demonstrating good statistical consistency.

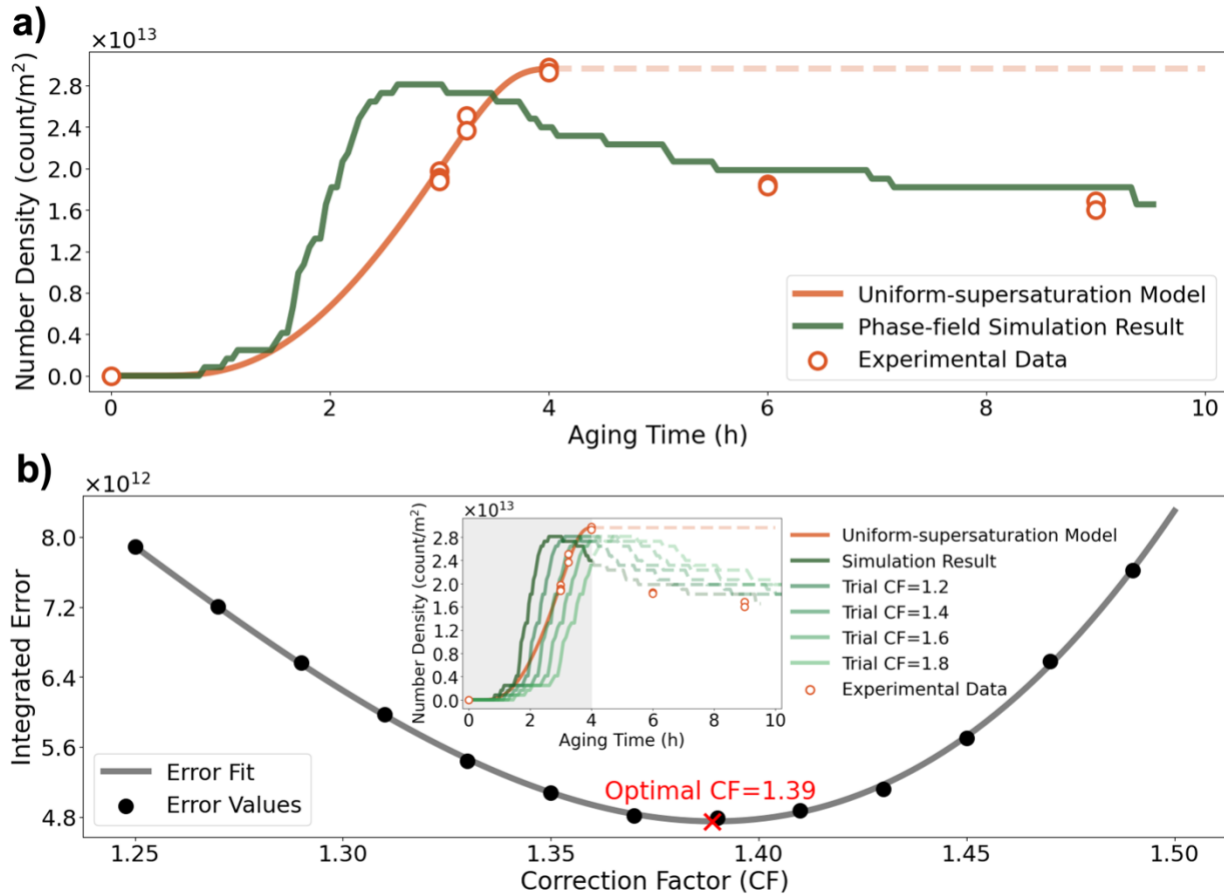


Figure 3. (a) Predicted number density versus aging time by the phase-field model before correction (green curve), in comparison with experimental data (open orange circles) and the uniform-supersaturation model's nucleation curve (orange curve) optimized against the experimental results. (b) Absolute differences between various trial-corrected number densities and the uniform-supersaturation model prediction that closely agree with experiment, integrated up to 4 hours (gray shaded in the inset), plotted as a function of correction factor (CF). The gray curve is a third-order polynomial fit used to determine the optimal CF, which corresponds to the minimum integration error. The subplot displays the number density as a function of time as in (a), with trial-corrected number density curves shown in various shades of green.

4.5. Simulation results and comparison with experimental data

After fine-tuning the model parameters, the simulations produce a quantitative prediction of precipitate number density as a function of aging time, in reasonable agreement with the effective 2D number densities calculated from the experimental data. Three independent simulations were

conducted using the same initially optimized nucleation rate parameters but using different sets of random numbers, each corrected by its optimal CF. The results are statistically consistent, as shown in figure 4. Several representative aging times are labeled as t_0 – t_8 in figures 4 and 5: 0.00 h, 1.47 h, 2.03 h, 2.52 h, 3.01 h, 3.22 h, 3.99 h, 6.03 h, and 9.04 h. In figure 4(a), it can be observed that the precipitate number density increases significantly between t_1 to t_5 and decreases after t_6 , similarly to the effective 2D number densities (open orange circles). The increase in number density is attributed to nucleation at early times, followed by a decrease due to coarsening. Figure 5 shows the corresponding changes in microstructure, supporting the trend in number density evolution. Some discrepancies from the experimental data remain, particularly during coarsening. We expect these discrepancies to arise from stochastic effects in the nucleus seeding method and the difference in dimensionality, as well as experimental uncertainties such as measurement errors. Figure 4(b) shows the simulated precipitate area fraction as a function of time. The total area of precipitates was calculated by numerically integrating the sum of the order parameters over the simulation domain. As expected, when coarsening becomes dominant after t_6 , the precipitate area fraction remains nearly constant. A comparison of the average matrix Nd composition with the APT measurement is presented in figure 4(c). For the purpose of calculating the average matrix composition, only regions where the sum of order parameters is less than 0.001 are considered. The simulated Nd compositions fall within the statistical uncertainties of the majority of the experimental measurements.

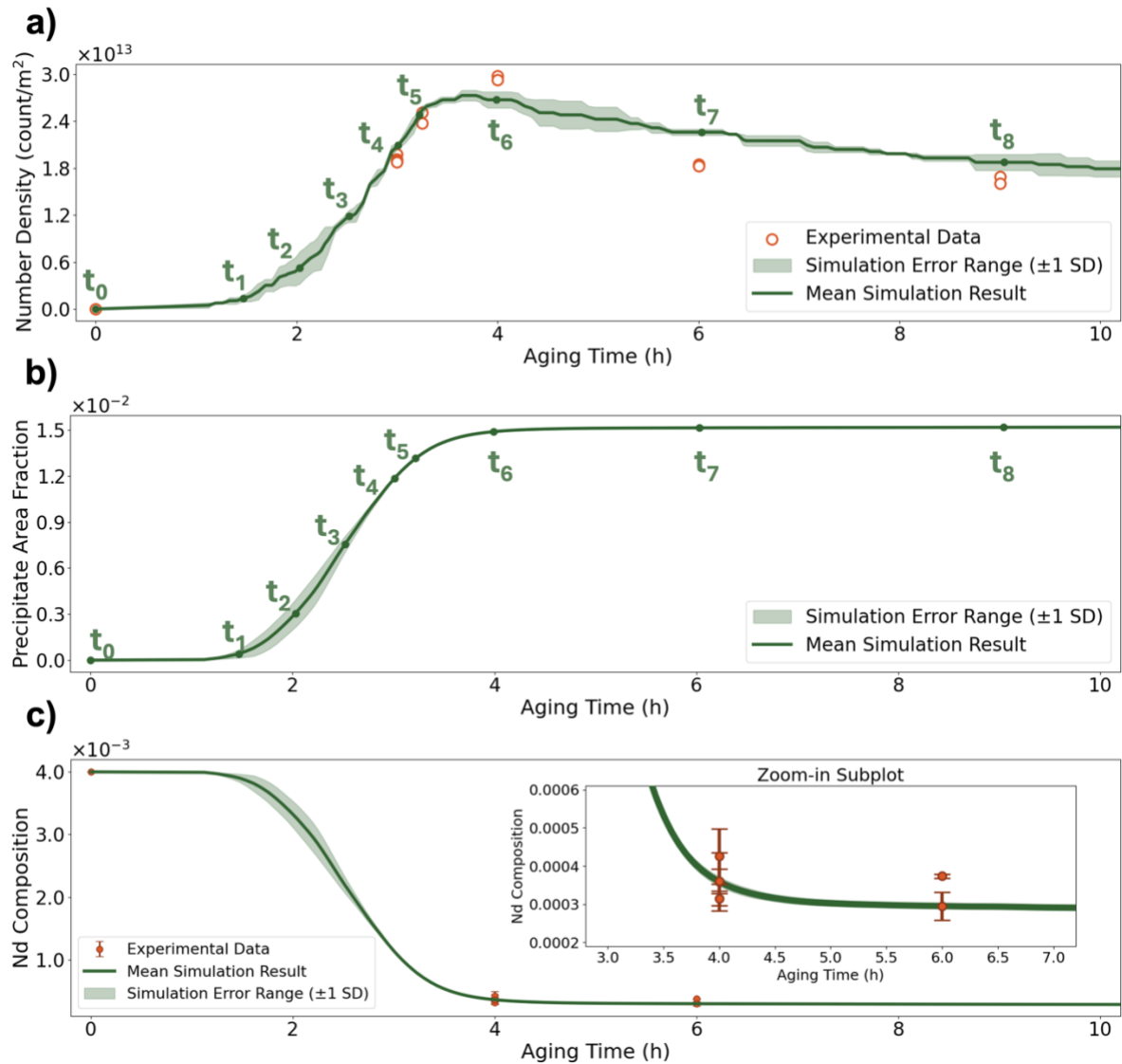


Figure 4. (a) Simulated number density as a function of aging time, along with the effective 2D number densities calculated from the experimental data (open orange circles). (b) Simulated precipitate area fraction as a function of aging time. (c) Simulated average Nd composition in the matrix as a function of aging time, compared with experimental APT measurements (filled orange circles, with error bars showing the statistical uncertainties). The inset shows a magnified view for 3–7 h. For all plots, solid green lines and shaded regions represent the mean and ± 1 standard deviation (SD) of 3 independent simulations, respectively.

Representative snapshots of the microstructure from the simulation for which the number density result was presented in figure 3 are shown in figure 5 for aging times t_0 – t_8 . The plate-like morphologies of β_1 precipitates with a habit plane of $\{1\bar{1}00\}_\alpha$ in the matrix is reproduced in

simulations. All six precipitate growth directions, consistent with the three deformation variants and their two orientation variants, are observed in the simulations, which agrees with experiments. This is notable since the model did not account for interfacial energy anisotropy; the results are solely due to anisotropic elastic properties.

The microstructural evolution exhibits different kinetic stages. Nucleation of β_1 precipitates occurs gradually in the matrix in regions of higher solute supersaturation, with a time-dependent rate consistent with the incubation period. In the early stage (before t_2), the nucleation rate is relatively slow, with only a few nucleation events observed. These nuclei experience significant longitudinal growth in size during this period. Subsequently, a transition to a rapid nucleation regime occurs between t_2 and t_6 , characterized by a sharp increase in the population of new, smaller precipitates. Beyond t_6 , the system enters a coarsening regime, in which some small precipitates gradually dissolve, allowing larger precipitates to grow. The simulations qualitatively reproduced these key features of the microstructure evolution, consistent with experimental results. A video showing the evolution of simulated number density and microstructure side by side is provided as figure S2 of the SI, offering a dynamic view of microstructural evolution during the simulation. Representative microstructure snapshots from all three independent simulations are presented in figure S3.

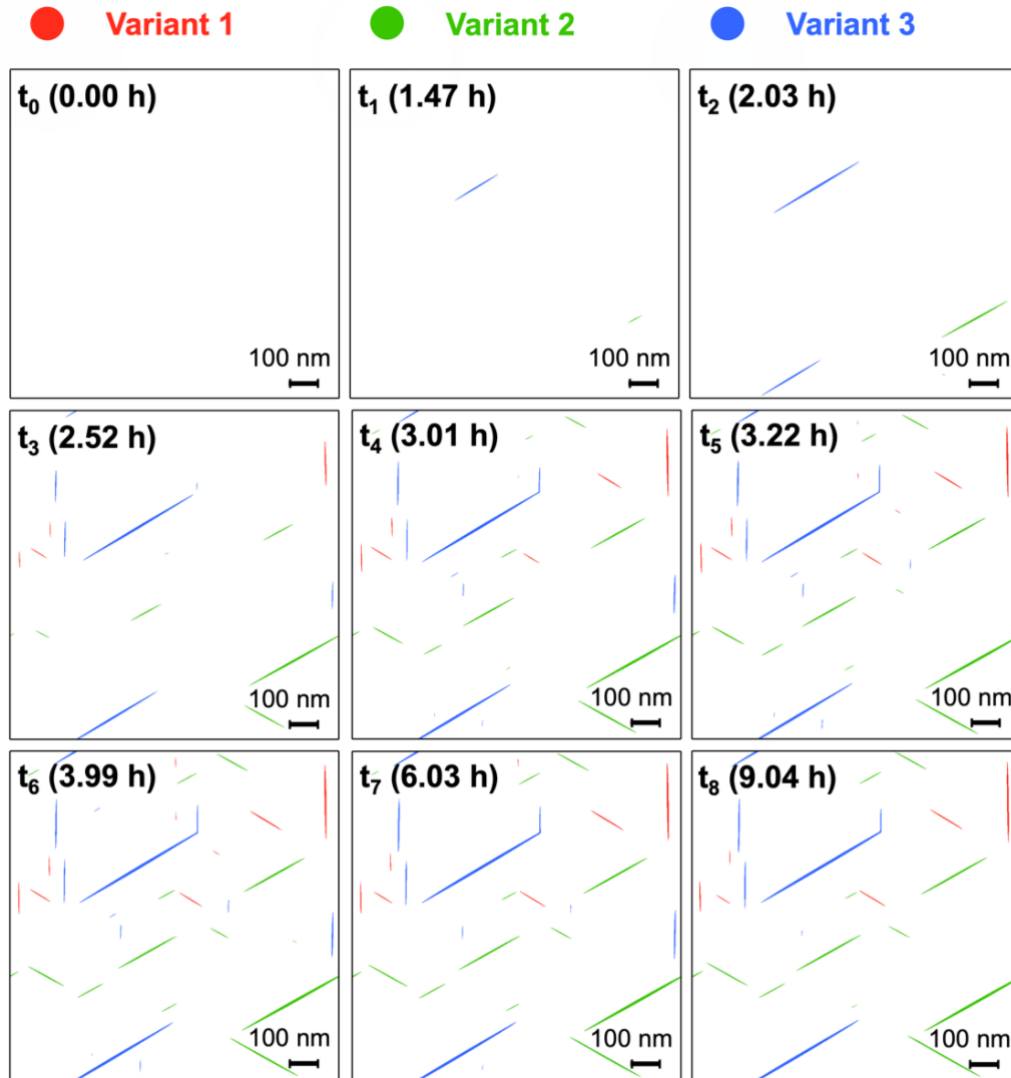


Figure 5. Simulated microstructure snapshots at selected aging times (t_0 – t_8 in figure 4), with different colors representing distinct precipitate variants of the β_1 precipitates.

The growth of nuclei is strongly influenced by local solute diffusion fields. Figure 6 shows the matrix composition at 2.31 h, 3.01 h, and 4.08 h for the same simulation. By 2.31 h, significant spatial variations in the supersaturation arise due to the few precipitates that have formed early and grown large. Once the incubation time has passed, nuclei form rapidly (t_2 – t_6); depending on where they form, their growth can already be suppressed, as solute may be depleted by the precipitates formed earlier. For example, two small precipitates having similar sizes at 2.31 h are highlighted in Figure 6, one with a solid red oval and the other with a dashed red oval. By 3.01 h, the precipitate marked with dashed oval grows significantly larger than the solid-oval one, which has

more neighbors competing for solute, one of which formed early (before t_2) and has grown very large. On the other hand, the precipitate marked with a dashed red oval formed away from other precipitates, and thus it is able to grow to much larger size. As the supersaturation decreases overall toward the late stage of the rapid nucleation, nuclei seeded have overall suppressed growth rates compared to the few initial nuclei formed before t_2 . Due to this depletion, neither of the two precipitates experiences significant growth from 3.01 h to 4.06 h. By the latter time, nucleation ceases, growth slows, and the coarsening stage begins.

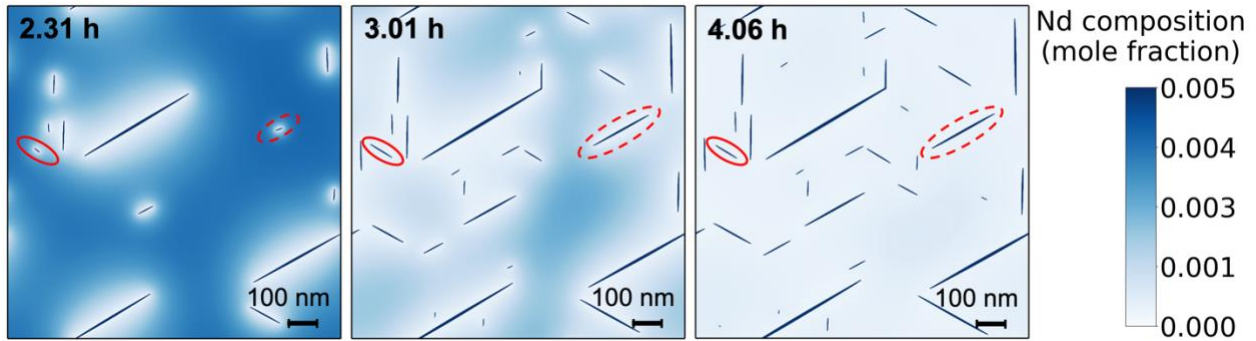


Figure 6. Nd composition at 2.31 h, 3.01 h and 4.06 h. To better contrast the precipitates and the matrix, a maximum value of 0.005 was used in the colorbar, while the maximum possible matrix composition is 0.004. Composition values greater than 0.005 were truncated. A solid red circle and a dashed red circle in the plots highlight two precipitates of comparable size at 2.31 h, which experience different growth rates and exhibit significant size difference at 3.01 h. The 4.06 h snapshot shows the depletion of solute supersaturation in the matrix as nucleation and growth progress.

5. Conclusions

In this work, we developed and validated a workflow that combines experimental measurements and literature data to enable parameterization of a 2D phase-field model for nucleation, growth, and coarsening of β_1 precipitates in Mg–Nd alloys. The workflow enables parameterization of the model, which incorporates a stochastic nucleation method, and addresses the challenges associated with limited input data, especially in modeling the nucleation stage. The resulting parameterized model captures both the evolution of individual morphologies of the β_1 precipitates, as well as the overall evolution of the precipitate microstructure. Specifically, we examined the evolution of precipitate number density determined from experiments, in which a rapid increase in number of

precipitates is observed during the nucleation stage followed by a slow decrease during the coarsening stage observed in the TEM measurements. Although the data for the average Nd composition of the matrix measured by APT were sparse, the simulation values were in excellent agreement with the data within the statistical uncertainty, where available.

The limitations of this study primarily arise from necessary modeling approximations. Primarily, 2D simulations that use the effective 2D number densities derived from estimated 3D experimental data cannot capture the full geometric complexity of interactions between precipitates, which may be important in determining microstructure evolution. In addition, using the uniform-supersaturation model to conduct the initial optimization of the nucleation parameters and then applying a single time-scale correction factor to the kinetic parameters of the model, D , ρ_1 , and τ_{in} , constraints the parameter space for optimization. This can lead to a suboptimal parameter set. However, this approach circumvents the need to perform a full sensitivity analysis, which can greatly increase the computational cost due to the large number of phase-field simulations that would be required.

Our workflow that uses experimental data to obtain model parameters and applies the parameterized model to the evolution of microstructure provides a robust framework that can be 1) employed to optimize the aging time for desired microstructures and 2) extended to study precipitation phenomena in a wide range of alloy systems beyond the β_1 phase in Mg–Nd alloys and for different aging conditions. We believe our results can be improved by performing experimental measurements of both composition and precipitate number density with a higher frequency during aging, particularly during the nucleation stage. This will provide more data to fit to and allow us to find the optimal model parameters with higher precision. In addition, the framework could benefit from incorporating a Bayesian method to perform an unconstrained parameter optimization while limiting the number of phase-field simulations required to find optimal model parameters, thereby reducing computational costs. Finally, a combination of 3D simulations and 3D characterization will be required to fully understand the complex interplay between thermodynamics, interfacial and elastic anisotropies, and the kinetics of nucleation, growth, and coarsening in Mg–Nd and other Mg–RE alloys. The methodology presented here provides a foundation on which these extensions can be built.

Acknowledgements

This work is supported by the U.S. Department of Energy, Office of Basic Energy Sciences, Division of Materials Sciences and Engineering, under Award No. DE-SC0008637 as part of the Center for Predictive Integrated Structural Materials Science (PRISMS Center) at the University of Michigan. This work used the allocation MSS160003 from the Advanced Cyberinfrastructure Coordination Ecosystem: Services & Support (ACCESS) program, which is supported by National Science Foundation grants #2138259, #2138286, #2138307, #2137603, and #2138296. This research also used resources of the National Energy Research Scientific Computing Center (NERSC), a Department of Energy User Facility, using NERSC award BES-ERCAP 0027826.

The authors gratefully acknowledge Dr. Zhihua Huang and Prof. Amit Misra for providing TEM measurements and related data, as well as for helpful discussions that contributed to improving this work.

References

- [1] J. F. Song, J. She, D. L. Chen, and F. S. Pan, "Latest research advances on magnesium and magnesium alloys worldwide," (in English), *J Magnes Alloy*, vol. 8, no. 1, pp. 1-41, Mar 2020, doi: 10.1016/j.jma.2020.02.003.
- [2] G. H. Wu, C. L. Wang, M. Sun, and W. J. Ding, "Recent developments and applications on high-performance cast magnesium rare-earth alloys," (in English), *J Magnes Alloy*, vol. 9, no. 1, pp. 1-20, Jan 15 2021, doi: 10.1016/j.jma.2020.06.021.
- [3] A. Issa, J. E. Saal, and C. Wolverton, "Formation of high-strength β' precipitates in Mg-RE alloys: The role of the Mg/ β' interfacial instability," (in English), *Acta Mater*, vol. 83, pp. 75-83, Jan 15 2015, doi: 10.1016/j.actamat.2014.09.024.
- [4] T. M. Pollock, "Weight Loss with Magnesium Alloys," (in English), *Science*, vol. 328, no. 5981, pp. 986-987, May 21 2010, doi: 10.1126/science.1182848.
- [5] Y. F. Li *et al.*, "Recent advances of high strength Mg-RE alloys: Alloy development, forming and application," (in English), *J Mater Res Technol*, vol. 26, pp. 2919-2940, Sep-Oct 2023, doi: 10.1016/j.jmrt.2023.08.055.
- [6] D. Han, J. Zhang, J. F. Huang, Y. Lian, and G. Y. He, "A review on ignition mechanisms and characteristics of magnesium alloys," (in English), *J Magnes Alloy*, vol. 8, no. 2, pp. 329-344, Jun 2020, doi: 10.1016/j.jma.2019.11.014.
- [7] H. Zengin and A. W. Hassel, "Magnesium alloys with rare earth elements - A review of the recent progress on the corrosion properties," (in English), *Corros Sci*, vol. 249, Jun 2025, doi: ARTN 112827
10.1016/j.corsci.2025.112827.

- [8] A. R. Natarajan, E. L. S. Solomon, B. Puchala, E. A. Marquis, and A. Van der Ven, "On the early stages of precipitation in dilute Mg-Nd alloys," (in English), *Acta Mater*, vol. 108, pp. 367-379, Apr 15 2016, doi: 10.1016/j.actamat.2016.01.055.
- [9] E. L. S. Solomon, V. Araullo-Peters, J. E. Allison, and E. A. Marquis, "Early precipitate morphologies in Mg-Nd-(Zr) alloys," (in English), *Scripta Mater*, vol. 128, pp. 14-17, Feb 2017, doi: 10.1016/j.scriptamat.2016.09.015.
- [10] J. H. Zhang, S. J. Liu, R. Z. Wu, L. G. Hou, and M. L. Zhang, "Recent developments in high-strength Mg-RE-based alloys: Focusing on Mg-Gd and Mg-Y systems," (in English), *J Magnes Alloy*, vol. 6, no. 3, pp. 277-291, Sep 2018, doi: 10.1016/j.jma.2018.08.001.
- [11] J. M. Meier, J. Caris, and A. A. Luo, "Towards high strength cast Mg-RE based alloys: Phase diagrams and strengthening mechanisms," (in English), *J Magnes Alloy*, vol. 10, no. 6, pp. 1401-1427, Jun 2022, doi: 10.1016/j.jma.2022.03.008.
- [12] T. L. Chia, M. A. Easton, S. M. Zhu, M. A. Gibson, N. Birbilis, and J. F. Nie, "The effect of alloy composition on the microstructure and tensile properties of binary Mg-rare earth alloys," (in English), *Intermetallics*, vol. 17, no. 7, pp. 481-490, Jul 2009, doi: 10.1016/j.intermet.2008.12.009.
- [13] S. Tekumalla, S. Seetharaman, A. Almajid, and M. Gupta, "Mechanical Properties of Magnesium-Rare Earth Alloy Systems: A Review," (in English), *Metals-Basel*, vol. 5, no. 1, pp. 1-39, Mar 2015, doi: 10.3390/met5010001.
- [14] H. Karimzadeh, "The microstructure and mechanical properties of some magnesium alloys containing yttrium and heavy rare earths," University of Manchester, 1985.
- [15] J. F. Nie and B. C. Muddle, "Characterisation of strengthening precipitate phases in a Mg-Y-Nd alloy," (in English), *Acta Mater*, vol. 48, no. 8, pp. 1691-1703, May 11 2000, doi: Doi 10.1016/S1359-6454(00)00013-6.
- [16] Y. Z. Ji, A. Issa, T. W. Heo, J. E. Saal, C. Wolverton, and L. Q. Chen, "Predicting β' precipitate morphology and evolution in Mg-RE alloys using a combination of first-principles calculations and phase-field modeling," (in English), *Acta Mater*, vol. 76, pp. 259-271, Sep 1 2014, doi: 10.1016/j.actamat.2014.05.002.
- [17] H. Liu, Y. Gao, Y. M. Zhu, Y. Wang, and J. F. Nie, "A simulation study of β_1 precipitation on dislocations in an Mg-rare earth alloy," (in English), *Acta Mater*, vol. 77, pp. 133-150, Sep 15 2014, doi: 10.1016/j.actamat.2014.04.054.
- [18] S. DeWitt *et al.*, "Misfit-driven β'' precipitate composition and morphology in Mg-Nd alloys," (in English), *Acta Mater*, vol. 136, pp. 378-389, Sep 1 2017, doi: 10.1016/j.actamat.2017.06.053.
- [19] Y. M. Zhu, H. Zhang, S. W. Xu, and J. F. Nie, "The β_1/β' Triad-Related Configurations in a Mg-RE Alloy," (in English), *Metall Mater Trans A*, vol. 51, no. 4, pp. 1887-1896, Apr 2020, doi: 10.1007/s11661-020-05651-1.
- [20] I. M. Lifshitz and V. V. Slyozov, "The kinetics of precipitation from supersaturated solid solutions," *Journal of Physics and Chemistry of Solids*, vol. 19, no. 1, pp. 35-50, 1961/04/01/ 1961, doi: [https://doi.org/10.1016/0022-3697\(61\)90054-3](https://doi.org/10.1016/0022-3697(61)90054-3).
- [21] A. Baldan, "Review Progress in Ostwald ripening theories and their applications to nickel-base superalloys Part I: Ostwald ripening theories," *Journal of Materials Science*, vol. 37, no. 11, pp. 2171-2202, 2002/06/01 2002, doi: 10.1023/A:1015388912729.
- [22] W. K. Yang, X. A. Jiang, X. L. Tian, H. Hou, and Y. H. Zhao, "Phase-field simulation of nano- α' precipitates under irradiation and dislocations," (in English), *J Mater Res Technol*, vol. 22, pp. 1307-1321, Jan-Feb 2023, doi: 10.1016/j.jmrt.2022.11.165.

- [23] H. Liu, Y. P. Gao, L. Qi, Y. Z. Wang, and J. F. Nie, "Phase-Field Simulation of Orowan Strengthening by Coherent Precipitate Plates in an Aluminum Alloy," (in English), *Metall Mater Trans A*, vol. 46a, no. 7, pp. 3287-3301, Jul 2015, doi: 10.1007/s11661-015-2895-3.
- [24] Y. Z. Ji, B. Ghaffari, M. Li, and L. Q. Chen, "Phase-field modeling of θ' precipitation kinetics in 319 aluminum alloys," (in English), *Comp Mater Sci*, vol. 151, pp. 84-94, Aug 2018, doi: 10.1016/j.commatsci.2018.04.051.
- [25] Z. Huang, J. E. Allison, and A. Misra, "Interaction of Glide Dislocations with Extended Precipitates in Mg-Nd alloys," *Scientific Reports*, vol. 8, no. 1, p. 3570, 2018/02/23 2018, doi: 10.1038/s41598-018-20629-1.
- [26] Z. Huang, C. Yang, L. Qi, J. E. Allison, and A. Misra, "Dislocation pile-ups at β_1 precipitate interfaces in Mg-rare earth (RE) alloys," *Materials Science and Engineering: A*, vol. 742, pp. 278-286, 2019/01/10/ 2019, doi: <https://doi.org/10.1016/j.msea.2018.10.104>.
- [27] E. E. Underwood, *Quantitative Stereology*. Addison-Wesley Publishing Company, 1970.
- [28] M. Hättestrand and H. O. Andrén, "Evaluation of particle size distributions of precipitates in a 9% chromium steel using energy filtered transmission electron microscopy," (in English), *Micron*, Review vol. 32, no. 8, pp. 789-797, Dec 2001, doi: 10.1016/s0968-4328(00)00086-x.
- [29] B. Sonderegger, "Modifications of stereological correction methods for precipitate parameters using transmission microscopy," *Ultramicroscopy*, vol. 106, no. 10, pp. 941-950, 2006/08/01/ 2006, doi: <https://doi.org/10.1016/j.ultramic.2006.04.004>.
- [30] S. G. Kim, W. T. Kim, and T. Suzuki, "Phase-field model for binary alloys," *Physical Review E*, vol. 60, no. 6, pp. 7186-7197, 12/01/ 1999, doi: 10.1103/PhysRevE.60.7186.
- [31] J. D. Eshelby, "The determination of the elastic field of an ellipsoidal inclusion, and related problems," *Proceedings of the Royal Society of London. Series A. Mathematical and Physical Sciences*, vol. 241, pp. 376 - 396, 1957.
- [32] A. G. Khachaturyan, *Theory of Structural Transformations in Solids*. Dover Publications, 2013.
- [33] J. W. Cahn and J. E. Hilliard, "Free Energy of a Nonuniform System. I. Interfacial Free Energy," *The Journal of Chemical Physics*, vol. 28, no. 2, pp. 258-267, 1958, doi: 10.1063/1.1744102.
- [34] S. M. Allen and J. W. Cahn, "Ground state structures in ordered binary alloys with second neighbor interactions," *Acta Metallurgica*, vol. 20, no. 3, pp. 423-433, 1972/03/01/ 1972, doi: [https://doi.org/10.1016/0001-6160\(72\)90037-5](https://doi.org/10.1016/0001-6160(72)90037-5).
- [35] A. M. Jokisaari, C. Permann, and K. Thornton, "A nucleation algorithm for the coupled conserved–nonconserved phase field model," *Comp Mater Sci*, vol. 112, pp. 128-138, 2016/02/01/ 2016, doi: <https://doi.org/10.1016/j.commatsci.2015.10.009>.
- [36] J. P. Simmons, C. Shen, and Y. Wang, "Phase field modeling of simultaneous nucleation and growth by explicitly incorporating nucleation events," *Scripta Mater*, vol. 43, no. 10, pp. 935-942, 2000/10/30/ 2000, doi: [https://doi.org/10.1016/S1359-6462\(00\)00517-0](https://doi.org/10.1016/S1359-6462(00)00517-0).
- [37] J. W. Christian, *The Theory of Transformations in Metals and Alloys: Equilibrium and general kinetic theory*. Elsevier Science & Technology, 1975.
- [38] S. DeWitt, S. Rudraraju, D. Montiel, W. B. Andrews, and K. Thornton, "PRISMS-PF: A general framework for phase-field modeling with a matrix-free finite element method," *npj*

- Computational Materials*, vol. 6, no. 1, p. 29, 2020/03/26 2020, doi: 10.1038/s41524-020-0298-5.
- [39] M. D. Abràmoff, P. J. Magalhães, and S. J. Ram, "Image processing with ImageJ," *Biophotonics international*, vol. 11, no. 7, pp. 36-42, 2004.
- [40] F. Danoix, G. Grancher, A. Bostel, and D. Blavette, "Standard deviations of composition measurements in atom probe analyses. Part I conventional 1D atom probe," (in eng), *Ultramicroscopy*, vol. 107, no. 9, pp. 734-8, Sep 2007, doi: 10.1016/j.ultramic.2007.02.006.
- [41] D. J. Larson, T. J. Prosa, R. M. Ulfing, B. P. Geiser, T. F. Kelly, and P. S. C. J. Humphreys, *Local Electrode Atom Probe Tomography: A User's Guide*. Springer New York, 2013.
- [42] M. K. Miller, "Data Representations and Analysis," in *Atom Probe Tomography: Analysis at the Atomic Level*, M. K. Miller Ed. Boston, MA: Springer US, 2000, pp. 157-195.
- [43] B. Gault, M. P. Moody, J. M. Cairney, and S. P. Ringer, "Analysis Techniques for Atom Probe Tomography," in *Atom Probe Microscopy*, B. Gault, M. P. Moody, J. M. Cairney, and S. P. Ringer Eds. New York, NY: Springer New York, 2012, pp. 213-297.
- [44] H. Y. Qi, G. X. Huang, H. Bo, G. L. Xu, L. B. Liu, and Z. P. Jin, "Thermodynamic description of the Mg–Nd–Zn ternary system," *Journal of Alloys and Compounds*, vol. 509, no. 7, pp. 3274-3281, 2011/02/17/ 2011, doi: <https://doi.org/10.1016/j.jallcom.2010.07.056>.
- [45] M. Paliwal, S. K. Das, J. Kim, and I.-H. Jung, "Diffusion of Nd in hcp Mg and interdiffusion coefficients in Mg–Nd system," *Scripta Mater*, vol. 108, pp. 11-14, 2015/11/01/ 2015, doi: <https://doi.org/10.1016/j.scriptamat.2015.06.010>.
- [46] C. Niu, M. Liu, C. Li, Z. Du, and C. Guo, "Thermodynamic description on the miscibility gap of the Mg-based solid solution in the Mg–Zn, Mg–Nd and Mg–Zn–Nd systems," *Calphad*, vol. 34, no. 4, pp. 428-433, 2010/12/01/ 2010, doi: <https://doi.org/10.1016/j.calphad.2010.07.010>.
- [47] Y.-B. Kang, L. Jin, P. Chartrand, A. E. Gheribi, K. Bai, and P. Wu, "Thermodynamic evaluations and optimizations of binary Mg-light Rare Earth (La, Ce, Pr, Nd, Sm) systems," *Calphad*, vol. 38, pp. 100-116, 2012/09/01/ 2012, doi: <https://doi.org/10.1016/j.calphad.2012.05.005>.
- [48] C. Guo, Z. Du, and C. Li, "Thermodynamic description of the Ce-Mg-Y and Mg-Nd-Y systems," *International Journal of Materials Research*, vol. 99, no. 6, pp. 650-688, 2008, doi: doi:10.3139/146.101685.
- [49] T. Luo, K. Zhu, H. Xiong, W. Zheng, J. Wang, and X.-G. Lu, "Thermodynamic Assessment of the Mg–La–Nd System," *Journal of Phase Equilibria and Diffusion*, vol. 46, no. 1, pp. 60-75, 2025/02/01 2025, doi: 10.1007/s11669-024-01169-w.
- [50] L. K. Aagesen *et al.*, "A phase-field model for void and gas bubble superlattice formation in irradiated solids," *Comp Mater Sci*, vol. 215, p. 111772, 2022/12/01/ 2022, doi: <https://doi.org/10.1016/j.commatsci.2022.111772>.
- [51] D. Choudhuri, R. Banerjee, and S. G. Srinivasan, "Interfacial structures and energetics of the strengthening precipitate phase in creep-resistant Mg-Nd-based alloys," *Scientific Reports*, vol. 7, no. 1, p. 40540, 2017/01/17 2017, doi: 10.1038/srep40540.
- [52] R. Storn and K. Price, "Differential Evolution – A Simple and Efficient Heuristic for global Optimization over Continuous Spaces," *Journal of Global Optimization*, vol. 11, no. 4, pp. 341-359, 1997/12/01 1997, doi: 10.1023/A:1008202821328.

- [53] P. Virtanen *et al.*, "SciPy 1.0: fundamental algorithms for scientific computing in Python," *Nature Methods*, vol. 17, no. 3, pp. 261-272, 2020/03/01 2020, doi: 10.1038/s41592-019-0686-2.
- [54] D. A. Porter and K. E. Easterling, *Phase Transformations in Metals and Alloys, Third Edition (Revised Reprint)*. Taylor & Francis, 1992.

Supplementary Information

S1. Approximate expression for ΔG^*

Consider the transformation from a solid-solution matrix phase, α , to a nucleus, β_1 in a small region. Following Ref. [54], upon removal of a small amount of material with the nucleus composition, $x_{Nd}^{\beta_1}$, from the α phase, the total free energy of the system per mole removed decreases by

$$\Delta G_m^1 = \mu_{Mg}^\alpha x_{Mg}^{\beta_1} + \mu_{Nd}^\alpha x_{Nd}^{\beta_1}, \quad (S1)$$

where x_i^j is the mole fraction of species i in phase j , and μ_i^j is the chemical potential of species i in phase j , defined as

$$\mu_i^j = \left(\frac{\partial G^j}{\partial N_i} \right)_{T,P,N_{k \neq i}}. \quad (S2)$$

The subscript m indicates that the quantity is per mole. In equation (S2), G^j is the contribution from phase j to the Gibbs free energy of the system, and N_i is the number of moles of species i . If the removed material transforms into the β_1 phase, the free energy of the system per mole added increases by

$$\Delta G_m^2 = \mu_{Mg}^{\beta_1} x_{Mg}^{\beta_1} + \mu_{Nd}^{\beta_1} x_{Nd}^{\beta_1}. \quad (S3)$$

Therefore, the driving force for nucleation is expressed as

$$\begin{aligned} \Delta G_m^{nuc} &= \Delta G_m^2 - \Delta G_m^1 \\ &= \left(\mu_{Mg}^{\beta_1} - \mu_{Mg}^\alpha \right) + \left[\left(\mu_{Nd}^{\beta_1} - \mu_{Nd}^\alpha \right) - \left(\mu_{Mg}^{\beta_1} - \mu_{Mg}^\alpha \right) \right] x_{Nd}^{\beta_1}. \end{aligned} \quad (S4)$$

The change of free energy per unit volume, ΔG_v , can be obtained from ΔG_m^{nuc} as

$$\Delta G_v = \frac{\Delta G_m^{nuc}}{V_m}, \quad (S5)$$

where V_m is the molar volume. The subscript v indicates that the quantity is per volume.

Considering that the transformation occurs within a constant volume and the pressure change is negligible, we can assume that the change in the Helmholtz free energy is approximately equal to that of the Gibbs free energy. We also assume that the nucleus composition, $x_{Nd}^{\beta_1}$, can be approximated by the equilibrium composition in the β_1 phase, $x_e^{\beta_1}$. As in Ref. [50], parabolic free

energy densities (equations (3) and (4)) of each phase are used, which determine the chemical potentials in equation (S4):

$$\mu_{Mg}^{\alpha} = f_{\alpha}(x_0) - x_0 \left. \frac{\partial f_{\alpha}(x_{Nd}^{\alpha})}{\partial x_{Nd}^{\alpha}} \right|_{x_{Nd}^{\alpha}=x_0} = -A_2(x_0)^2 + A_0; \quad (S6)$$

$$\begin{aligned} \mu_{Nd}^{\alpha} &= f_{\alpha}(x_0) + (1 - x_0) \left. \frac{\partial f_{\alpha}(x_{Nd}^{\alpha})}{\partial x_{Nd}^{\alpha}} \right|_{x_{Nd}^{\alpha}=x_0} \\ &= A_2[-(x_0)^2 + 2x_0] + A_1 + A_0; \end{aligned} \quad (S7)$$

$$\mu_{Mg}^{\beta_1} = f_{\alpha}(x_e^{\alpha}) - x_e^{\alpha} \left. \frac{\partial f_{\alpha}(x_{Nd}^{\alpha})}{\partial x_{Nd}^{\alpha}} \right|_{x_{Nd}^{\alpha}=x_e^{\alpha}} = -A_2(x_e^{\alpha})^2 + A_0; \quad (S8)$$

$$\begin{aligned} \mu_{Nd}^{\beta_1} &= f_{\alpha}(x_e^{\alpha}) + (1 - x_e^{\alpha}) \left. \frac{\partial f_{\alpha}(x_{Nd}^{\alpha})}{\partial x_{Nd}^{\alpha}} \right|_{x_{Nd}^{\alpha}=x_e^{\alpha}} \\ &= A_2[-(x_e^{\alpha})^2 + 2x_e^{\alpha}] + A_1 + A_0. \end{aligned} \quad (S9)$$

Here, x_e^{α} is the equilibrium composition in the matrix phase, and x_0 is the initial solute composition in the solid solution.

Substituting expressions (S6)–(S9) into (S4) yields

$$\begin{aligned} \Delta G_n &= (\mu_{Mg}^{\beta_1} - \mu_{Mg}^{\alpha}) + [(\mu_{Nd}^{\beta_1} - \mu_{Nd}^{\alpha}) - (\mu_{Mg}^{\beta_1} - \mu_{Mg}^{\alpha})] x_{Nd}^{\beta_1} \\ &= 2A_2(x_e^{\beta_1} - x_e^{\alpha}) \left[\frac{\Delta x}{2(x_e^{\beta_1} - x_e^{\alpha})} - 1 \right] \Delta x, \end{aligned} \quad (S10)$$

where $\Delta x = x_0 - x_e^{\alpha}$ is the supersaturation. In the Mg–Nd system studied, $\frac{\Delta x}{2(x_e^{\beta_1} - x_e^{\alpha})} \ll 1$ for the entire range of possible supersaturation values during aging. Thus, we approximate ΔG_v as proportional to Δx

$$\Delta G_v \approx - \frac{2A_2(x_e^{\beta_1} - x_e^{\alpha})}{V_m} \Delta x. \quad (S11)$$

S2. Comparison between ΔG_v and ΔG_{strain}

Assuming the system is initially unstrained, the change in strain energy of the system per volume of the nucleus upon its introduction, ΔG_{strain} , is

$$\Delta G_{strain} = \frac{1}{V_{nucleus}} \int_V f_{el} dV, \quad (S12)$$

where $V_{nucleus}$ is the volume of a single nucleus introduced to the Mg–Nd system, f_{el} is the elastic energy density that is introduced by the single nucleus across the simulation domain, V . For our 2D phase-field simulations, we have

$$\Delta G_{strain} = \frac{1}{A_{nucleus}} \int_A f_{el} dA, \quad (S13)$$

where $A_{nucleus}$ is the area of the nucleus. For the values of C_{ijkl} and ϵ_{ij}^0 reported in section 4.3, we obtained a value of $\Delta G_{strain} = 1.33 \times 10^8 \text{ J/m}^3$ from a 2D phase-field simulation for a seed size similar to the critical nucleus size.

Using the values of A_2 , $x_e^{\beta_1}$, x_e^α reported in section 4.3, along with $\Delta x = 3.70 \times 10^{-3}$ (which corresponds to the initial supersaturation in the system), we calculate $\Delta G_v = -1.44 \times 10^9 \text{ J/m}^3$, therefore, the neglecting the strain energy is a good assumption during the early stage of the nucleation stage. The last few seeded nuclei in the simulations occur in regions where Δx is around 0.001, which makes $\Delta G_v \approx -3.6 \times 10^8 \text{ J/m}^3$. This value is still smaller, though it indicates that strain energy may affect the nucleation rate toward the end of the simulation.

S3. Simplified expression for ΔG^* and ρ_2

We start from equation (16) for the nucleation rate from classical nucleation theory

$$J = ZN_n\beta \exp\left(-\frac{\Delta G^*}{kT}\right) \exp\left(-\frac{\tau_{in}}{t}\right), \quad (S14)$$

where

$$\Delta G^* = \frac{16\pi\gamma^3}{3(\Delta G_v - \Delta G_{strain})^2}. \quad (S15)$$

Neglecting the term G_{strain} and substituting the approximate expression for ΔG_v from equation (S11) into equation (S15), we obtain

$$\Delta G^* \simeq \frac{16\pi\gamma^3}{3\Delta G_v^2} = \frac{4\pi\gamma^3 V_m^2}{3(A_2)^2 (x_e^{\beta_1} - x_e^\alpha)^2 \Delta x^2}. \quad (S16)$$

Finally, substituting ΔG^* into equation (S14), we obtain

$$J(\mathbf{r}, t) = ZN_n\beta \exp\left(-\frac{\rho_2}{\Delta x^2}\right) \exp\left(-\frac{\tau_{in}}{t}\right), \quad (\text{S17})$$

with ρ_2 given by

$$\rho_2 = \frac{4\pi\gamma^3 V_m^2}{3kT(A_2)^2 (x_e^{\beta_1} - x_e^\alpha)^2}. \quad (\text{S18})$$

S4. Composition fit for initial estimation of the nucleation rate parameters

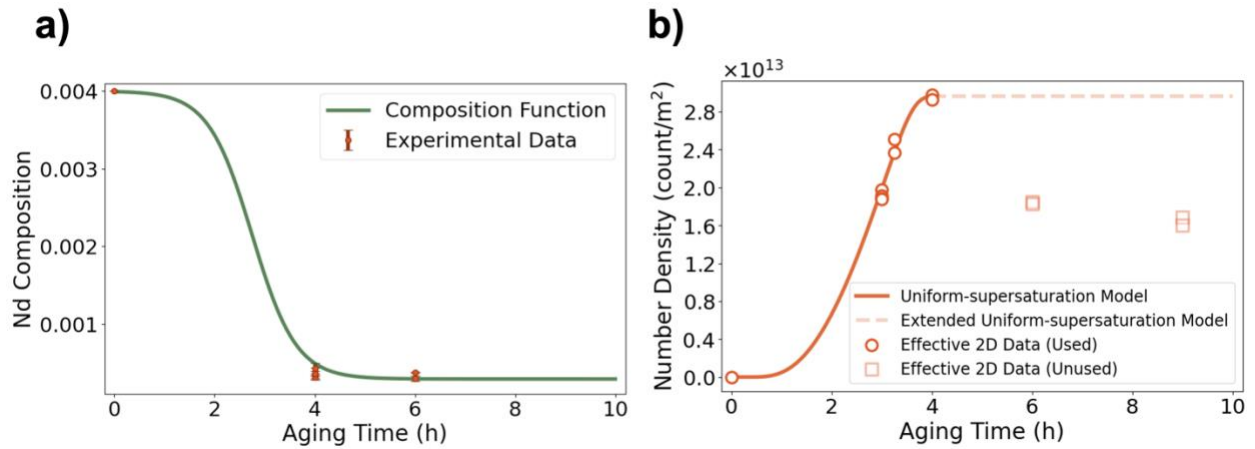


Figure S1. Fitted average matrix composition as a function of aging time, shown with experimental matrix composition data points.

S5. Evolution over time for fully parameterized model

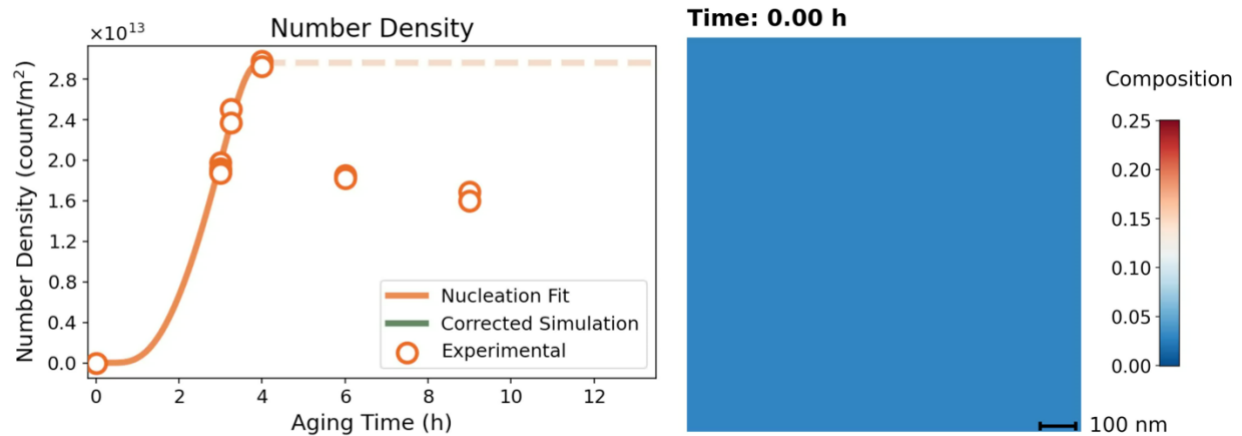


Figure S2. Video of simulated precipitate number density (left) and microstructure evolution (right) over time.

S6. Microstructures from different simulations

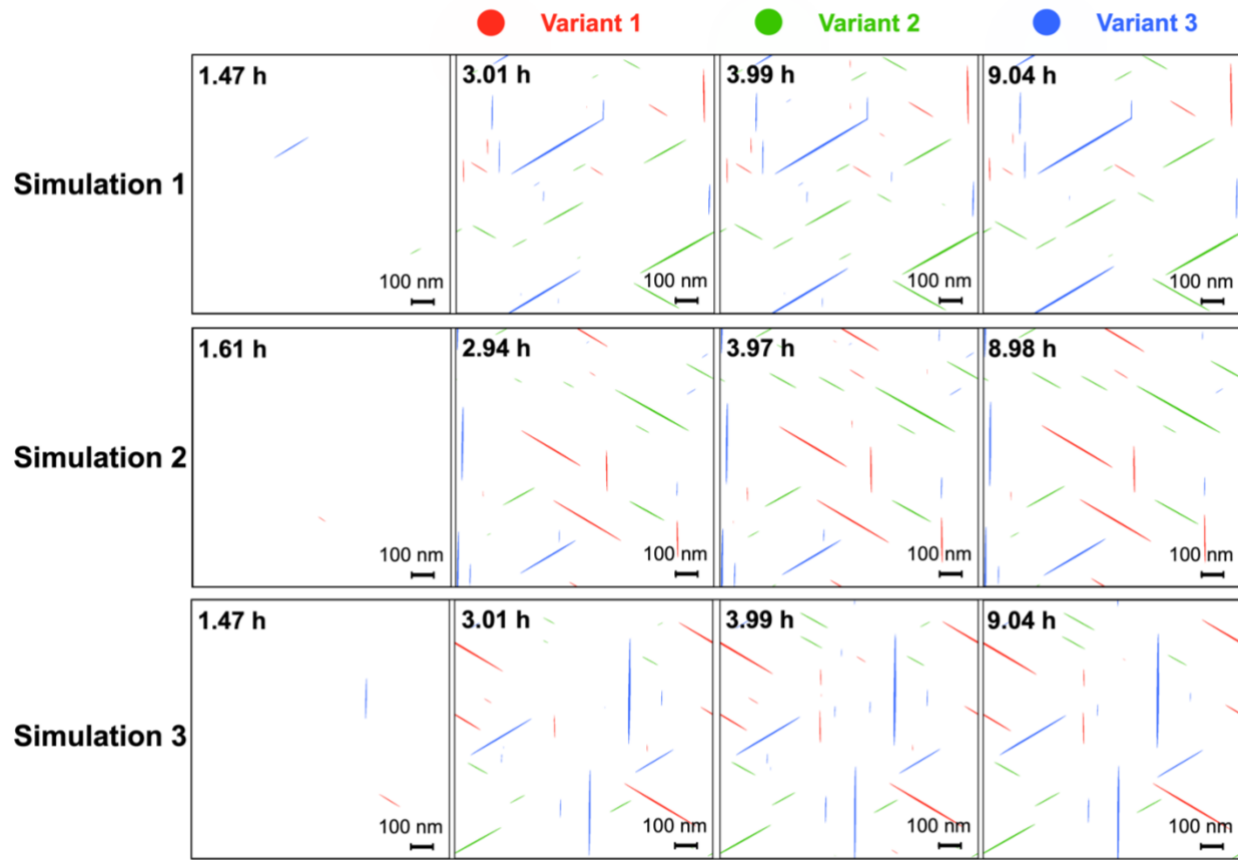


Figure S3. Simulated microstructure snapshots from three independent simulations at selected aging times, with different colors representing distinct precipitate variants of the β_1 precipitates. In Simulation 2, no nucleus was seeded before 1.61 h, while Simulations 1 and 3 experienced earlier nucleation.